IDŐJÁRÁS

QUARTERLY JOURNAL
OF THE HUNGARIAN METEOROLOGICAL SERVICE

CONTENTS

****

http://omsz.met.hu/english/ref/jurido/jurido_en.html

VOL. 108 * NO. 2 * APRIL – JUNE 2004

IDŐJÁRÁS

Quarterly Journal of the Hungarian Meteorological Service

Editorial Office: P.O. Box 39, H-1675 Budapest, Hungary or
Gilice tér 39, H-1181 Budapest, Hungary
E-mail: prager.t@met.hu or *antal.e@met.hu*
Fax: (36-1) 346-4809

Subscription by

mail: IDŐJÁRÁS, P.O. Box 39, H-1675 Budapest, Hungary;
E-mail: prager.t@met.hu or *antal.e@met.hu*; *Fax: (36-1) 346-4809*

IDŐJÁRÁS

Quarterly Journal of the Hungarian Meteorological Service
Vol. 108, No. 2, April–June 2004, pp. 79–94

Theoretical approach of a continuous flow particle counter by condensation of ambient humidity

Evelyne Géhin[1*] and **André Renoux**[2]

[1]*Centre d'Etudes et de Recherches en Thermique Environnement et Systèmes (CERTES), Université Paris XII, Avenue du Général de Gaulle, 94010 Créteil, France; E-mail: gehin@univ-paris12.fr*

[2]*Laboratoire de Physique des Aérosols et Transfert des Contaminations (LPATC), Université Paris XII, Avenue du Général de Gaulle, 94010 Créteil, France; E-mail: renoux@univ-paris12.fr*

(Manuscript received January 16, 2003; in final form October 6, 2003)

Abstract—A new principle of a continuous flow particle counter is presented. It uses the natural presence of water vapor in ambient air to cause particle growth by condensation. The water vapor condensation is started by a continuous subsonic expansion in a nozzle with its outlet set into vacuum by pumping. The reached saturation depends on relative air humidity, nozzle throat cross section, and parameters of the system (mass flow rate, downstream pressure, and upstream temperature). The COPACHA (Continuous Particle Counter by Condensation of Ambient Humidity) enables to detect particles with size equal to or larger than 10 nm for relative humidity >20%. Downstream pressure shall be between 600 and 700 hPa, and the minimum nozzle throat length must be 20 cm.

Key-words: CNC, heterogeneous condensation, growth rate, nozzle, air-water vapor expansion, saturation.

1. Introduction

Measurement of the atmospheric particulate pollution needs to take into consideration the ultrafine aerosol ($d_p < 0.1$ μm) more and more. For this aim, the Condensation Nucleus Counter (CNC) is the most suitable device as much

* Corresponding author

for the detection of this aerosol as for its size distribution measurement, in connection with an electrical aerosol analyzer or a diffusion battery (*Götz et al.*, 1991; *Renoux* and *Boulaud,* 1998). All CNCs are based on the principle of particle growth by condensation in order to make them detectable. Boulaud (*Renoux* and *Boulaud*, 1998) classified them into three categories according to the methods applied to induce the supersaturation: adiabatic expansion, mixing of cold and warm fluids, cooling by circulation in a cold-walled pipe. These different techniques have led to the development of many types of continuous or discontinuous flow CNCs (*McMurry*, 2000). Another classical technique to perform supersaturation is the process of expansion in a nozzle (*Stodola*, 1927). For example, this technique has been applied to produce monodispersed aerosols (*Turner et al.*, 1988) or superfine powders (*Tom* and *Debenedetti,* 1991). Several researchers have studied particle growth by heterogeneous condensation in a nozzle (*Johnston* and *Wexler*, 1995; *Mallina* and *Wexler*, 1997; *Yang et al.*, 2000a, *Jurski* and *Géhin,* 2003). Apparently, *Yang et al.* (2000b) have been the only ones until now, who used this method to design and perform a continuous operating type CNC. They mixed the initial aerosol with air saturated by clean water. The mixing was followed by expansion in a nozzle. In this way one can detect particles with a diameter exceeding 40 nm. According to the authors, this technique reduces losses due to diffusion, and there is little condensation on nozzle walls contrary to the systems involving wall cooling. Furthermore, let us add, that, as the velocity profile in a nozzle is practically flat, parameters such as temperature, total pressure, and vapor pressure show little variation within a given section, thus avoiding the necessity to consider the exact trajectory of the particle (in a classical CNC, particles are injected into the center to avoid variations due to the temperature profile in a given section of the condenser pipe). Consequently, this approach seems to be promising because of its simplicity, and we shall demonstrate that it can be further simplified by using ambient humidity naturally present in the air. Our system (COPACHA, Continuous Particle Counter by Condensation of Ambient Humidity, see *Fig. 1*) makes use of the natural presence of water vapor in ambient air to cause particle growth. Water vapor condensation on aerosol results from a continuous subsonic expansion in a nozzle with outlet set into vacuum by pumping. The saturation reached depends on relative humidity of air and operating parameters of the system (flow rate, downstream pressure, initial fluid temperature). It is possible to get saturation ratio around 3 by adjusting these parameters so that particles with diameter over 4 nanometers can theoretically be activated. The aerosol growth can be emphasized after activation by throat lengthening, that enables to increase the transit time and consequently the final diameter. The particles are detected at throat outlet by a classical system using light scattering.

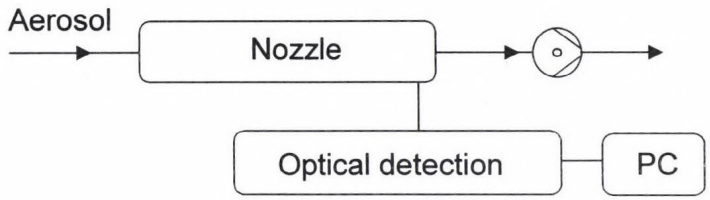

Fig. 1. COPACHA skeleton diagram.

2. Particle growth by condensation in a nozzle

Let us assume, that particles are spherical, uniformly distributed in the gas phase, and they are present in low concentration ($< 10^5$ particles cm^{-3}). Gas phase consists of a mixture of air and water vapor. As an indication, absolute humidity is under 0.015 kg of water kg^{-1} of dry air for moist air at standard atmospheric pressure and a temperature of 20°C. Because of the low water vapor content and particle concentration, we can consider the effect of drop or wall condensation upon the global parameters (total pressure, temperature, gas density) as insignificant. This approximation is justified (*Barrett* and *Clement*, 1986), when the particle concentration is low or the condensable mass is insignificant compared to total fluid mass. Then, the mix of both phases is processed as a pseudo-fluid, and the flow can be described by the same equations as those of a one phase flow.

The study of the compressible fluid flow in a nozzle is based on a few classical assumptions. Thus, we assume that the flow is one dimensional, permanent, adiabatic (low flow transit time in the nozzle justifies this considering that there are no exchanges with outside during expansion), the interactions with walls can be neglected (contact friction, thermal transfers), and the fluid is a perfect one. Under these circumstances, solving the equations of mass, motion, and energy conservation, as well as the fluid state equation, we obtain the classical expression of the variations of the different flow characteristics related to the Mach number (M_{ach}):

$$\left[1+\frac{(\gamma-1)}{2}M_{ach}{}^2\right]=\frac{T_i}{T}=\left(\frac{p_i}{p}\right)^{\left(\frac{\gamma-1}{\gamma}\right)}=\left(\frac{\rho_i}{\rho}\right)^{\gamma-1}, \quad M_{ach}=\frac{v}{a}, \quad a=\sqrt{\gamma r T}, \qquad (1)$$

where T_i, p_i, ρ_i are the temperature, pressure, density of the generating state, that is the characteristics of the fluid sampled at the entrance of the nozzle.

Further, T, p, ρ, M_{ach}, v are the temperature, pressure, density, Mach number, velocity of the fluid in a given nozzle section. a is the sound velocity. Finally, γ and r are the ratio of gas specific heats and the ideal gas constant. Furthermore, considering the above mentioned conditions:

$$p = p_{as} + p_v \approx p_{as}, \qquad \rho = \rho_{as} + \rho_v + \rho_a \approx \rho_{as}, \tag{2}$$

where the subscripts *as*, *v*, *a* denote dry air, vapor, and aerosol.

To Eq. (1), we must add the conservation of total mass flux rate, q, in every nozzle section:

$$q = \rho A v, \tag{3}$$

where A is the section area at a given nozzle section.

As the saturated vapor pressure, p_{vs}, is always low compared to total pressure, the saturation, S, is given by:

$$S \approx H = \frac{p_v}{p_{vs}}, \tag{4}$$

where H is the relative humidity of moist air. Water vapor pressure, p_v, in a given section of the nozzle is calculated for monodispersed aerosol with initial diameter, D_i, and by assuming of no extra condensation on the walls:

$$p_v = \left[\frac{p}{P_i} p_{vi}\right] - (D^3 - D_i^3)\frac{\pi \rho_l N}{6}\frac{r_{gp} T}{M_v}. \tag{5}$$

In this equation p_{vi} is the initial vapor pressure, D and N are the diameter and concentration of the droplet in the nozzle, while ρ_l, r_{gp}, and M_v are the water density, universal gas constant, and water vapor molecular mass, respectively. With the assumption of no coalescence phenomena or over losses in the nozzle, wich is a good approximation according to the short residence time of flowing particles in the system, N is calculated with the following equation:

$$N = N_i \frac{\rho}{\rho_i}. \tag{6}$$

2.1 Particle activation and critical saturation

Since there is no initial thermal unbalance between different phases, the Kelvin equation gives the minimum diameter of the nuclei activated at a given saturation and temperature:

$$D_{min} = \frac{4\,\sigma_l\,M_v}{\rho_l\,r\,T\,\ln(S)}. \tag{7}$$

In the case of soluble particle consisting of, for example, salt, the condensation process is initiated at saturation ratio lower than that described in Eq. (7), leading to a decrease of D_{min}. For non-wettable particles, the vapor tends to deposit in very small droplets; when the particle surface is completely covered, a uniform liquid film appears, the nucleus is then entirely coated (*Fletcher,* 1962). This phenomenon tend to increase the activation saturation and consequently D_{min}. In the first step this phenomenon is neglected and Eq. (7) will be used.

According to *Ahn* (1988), the critical saturation ratio, corresponding to the threshold at which the homogeneous condensation appears, can be determined by calculating the value of S for which $I = 1\ \mathrm{m^{-3}\ s^{-1}}$ (I is the nucleation rate). We obtain:

$$S_{cr} = \exp\left[\frac{16\,\pi}{3}\left(\frac{\sigma}{KT}\right)^3 \frac{v_m^2}{\ln\left(2v_m\left(\frac{p_v}{KT}\right)^2\left(\frac{\sigma}{2\pi m_v}\right)^{1/2}\right)}\right]^{1/2} \tag{8}$$

In this equation σ, v_m, and m_v are the surface tension, vapor molecule volume, and mass, respectively. This saturation factor shall not be exceeded, otherwise condensation nuclei could appear, resulting in an overestimation of the particle number.

2.2 Particle growth

Heat and mass transfer phenomena between particle and surrounding medium depend on Knudsen number:

$$Kn = \frac{2\lambda}{D},$$

where λ is the mean free path of carrying gas molecules. Calculations of Knudsen number for particles with a diameter of 10 nm gives values from 1 to 10 in our conditions. According to the classification given by *Devienne* (1958), the corresponding flow regime is consequently the transient one (Knudsen regime).

Diameter variation of a sphere is linked to J, the water vapor mass flow reaching the droplet:

$$\frac{dD}{dt} = \frac{J}{\frac{\pi}{2} D^2 \rho_l}. \tag{9}$$

Fuchs and *Sutugin* (1970) give the expression of water vapor mass flow reaching the drop for the transient regime. With the correction for relative motion between gas and droplet (*Hughmark,* 1967), J is given by:

$$J = C(Kn_v)\, Sh\, D_{vg}\, \pi D \left(\frac{p_{v\infty} M_v}{r_{gp} T_\infty} - \frac{p_{vd} M_v}{r_{gp} T_d} \right), \tag{10}$$

where $p_{v\infty}$, T_∞, p_{vd}, T_d are the vapor pressure and fluid temperature, respectively, far from the droplet and at the droplet surface.

$$p_{vd} = p_{vs}(T_d) \exp\left(\frac{4\sigma_l M_v}{\rho_l r_{gp} T_d D} \right), \tag{11}$$

where D_{vg} is the vapor diffusion coefficient in the gas (Appendix), while Sh is the Sherwood number (Appendix). In Eq. (10) $C(kn_v)$ is the Fuchs's correction coefficient defined by (*Fuchs,* 1959):

$$C(Kn_v) = \frac{1 + Kn_v}{1 + 1.7104\, Kn_v + \frac{4}{3} Kn_v^2} \quad \text{and} \quad Kn_v = \frac{2\lambda_v}{D}, \tag{12}$$

where λ_v is the mean free path of water vapor molecules in air. It is defined by the Meyer's formula:

$$\lambda_v = \frac{3 D_{vg}}{V}. \tag{13}$$

In Eq. (13) V is the average thermal velocity at temperature T:

$$V = \left(\frac{8KT}{\pi m_v} \right)^{1/2}, \tag{14}$$

where K is the Boltzmann constant, while m_v is the mass of a water molecule.

2.3 Particle temperature

If we assume an isothermal droplet and take into account the correction for relative motion, the droplet temperature evolution for Knudsen regime is given by:

$$\rho_l C_{pl} \frac{dT_d}{dt} = \frac{6}{\pi D^3}(Q_l - Q_c), \tag{15}$$

where C_{pl} is the specific heat at constant pressure for water, Q_c is the heat release by conduction in the gas, and Q_l is the condensation heat:

$$Q_c = \pi D k (T_d - T_\infty) C(kn) Nu, \tag{16}$$

$$Q_l = JL, \tag{17}$$

where Nu is the Nusselt number (Appendix), k is the thermal conductivity of gas, while $C(kn)$ is the Fuchs's correction coefficient for the carrying gas defined by:

$$C(kn) = \frac{1 + Kn}{1 + 1.7104 Kn + \frac{4}{3} Kn^2}. \tag{18}$$

2.4 Particle motion

Drag and pressure forces can be considered as the only external forces acting on flowing particles, then the particle motion can be described by the following equation:

$$\left(\frac{\pi D^3 \rho_l}{6}\right) \frac{dv_d}{dt} = -\frac{6\pi \mu C_D Re_d D}{48 C_c}(v_d - v) - \frac{dp}{dx}\frac{\pi D^3}{6}, \tag{19}$$

where Re_d is the droplet Reynolds number defined by:

$$Re_d = \frac{|v_d - v| D\rho}{\mu}. \tag{20}$$

Further, the values of the drag factor, C_D, are the following (*Kurten et al.*, 1966):

$$C_D = \begin{cases} \dfrac{24}{Re_d} & \text{for} \quad Re_d < 0.1 \\ 0.28 + \dfrac{6}{Re_d^{0.5}} + \dfrac{21}{Re_d} & \text{for} \quad 0.1 < Re_p < 4000 \end{cases} \tag{21}$$

Finally, in Eq. (19) C_c is the Cunningham factor. It can be expressed as a function of the particle diameter and mean free path of gas molecules, λ (*Seinfeld,* 1986):

$$C_c = 1 + \frac{2\lambda}{D}\left[1.257 + 0.4\exp\left(\frac{-1.1D}{2\lambda}\right)\right]. \tag{22}$$

2.5 Solving method

Fluid pressure, temperature, density, and velocity in the nozzle are first calculated with Eqs. (1), (2), (3). Then the particle concentration is estimated at each position in the nozzle with Eq. (6). Then, Eqs. (5), (9), (15), and (19) are solved at all points of the nozzle by the Runge-Kutta method.

3. Discussion

The aims of our study are to show that:

- saturation values, that can be reached by using this device in ambient air with relative humidity $>20\%$, enable us to activate particles with a diameter over 10 nm,
- saturation values reached remain under the critical saturation value,
- growth of activated particles is sufficient to have them detected.

In the calculations presented, we consider that the nozzle has a circular cross section and its diameter linearly varies from inlet diameter d_i to throat diameter d_{th} (*Fig. 2*). Pressure and temperature in generating state are $p_i = 10^5$ Pa and $T_i = 288$ K, respectively. We consider different throat lengths in order to obtain sufficient retention times for particles growth.

3.1 Particle activation in COPACHA

Fig. 3 shows how the saturation varies in relation to cross section ratios in the nozzle for different initial and downstream pressure ratios. The saturation ratio

remains almost constant for normalized sections over 1.4, but its variation becomes significant for normalized sections under 1.2. This indicates that condensation in the nozzle appears exclusively for sections very near to the nozzle throat. This phenomenon is confirmed by *Fig. 4*, that gives the variation of the minimal activation diameter in relation with the normalized section for different pressure drops. The activation of particles under 10 nm exclusively occurs for normalized sections under 1.15.

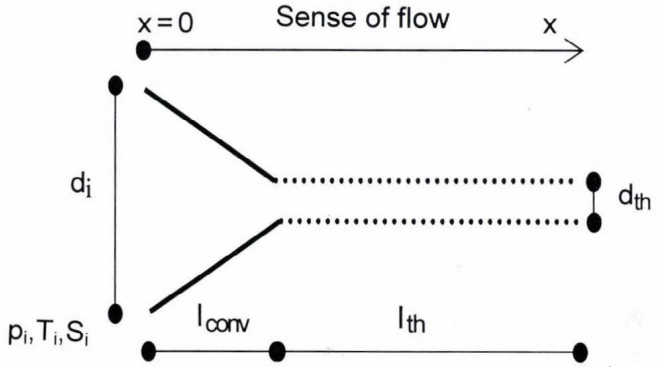

Fig. 2. Geometry used for theoretical study. p_i, T_i, S_i are the initial pressure, temperature, and saturation ratio, while d_i and d_{th} are the entrance and throat nozzle diameters, l_{conv} and l_{th} are the convergent zone and throat length, respectively.

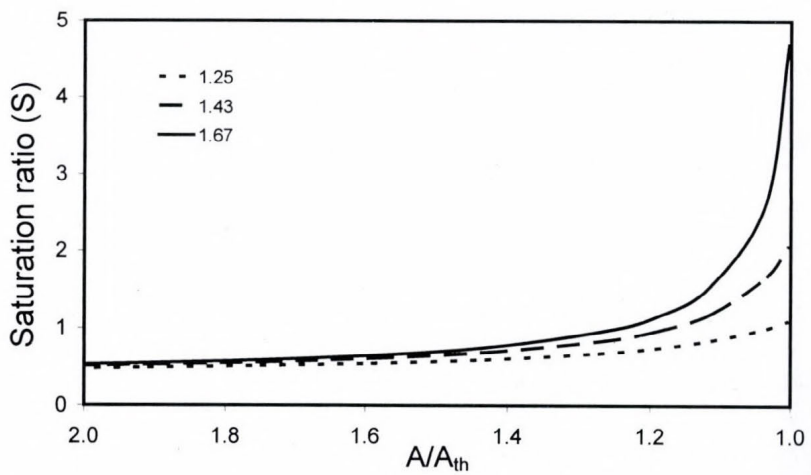

Fig. 3. Saturation in the nozzle (without condensation) in relation to section ratios (A/A_{th}) for different pressure drops ($p_i/p_{downstream}$), where $A_i/A_{th} = 796$, $S_i = 0.4$.

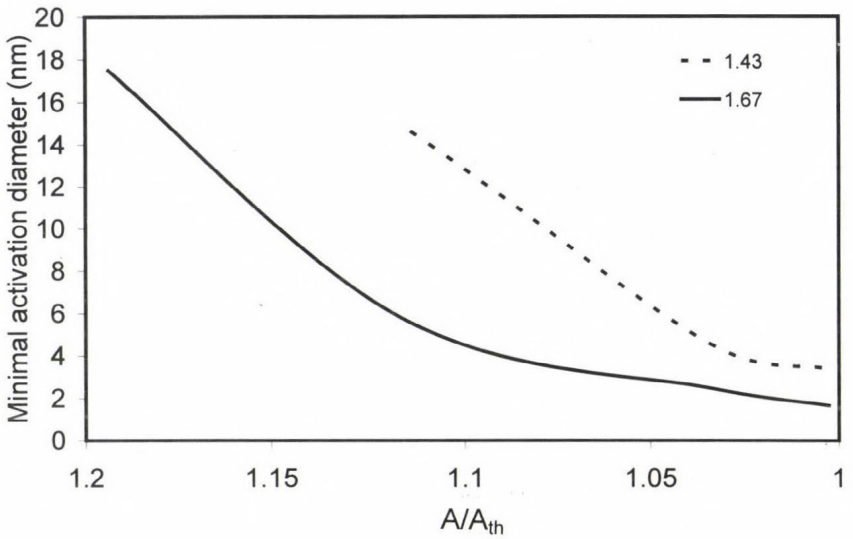

Fig. 4. Minimal activation diameter in relation to normalized section (A/A_{th}) for different pressure drops ($p_i/p_{downstream}$), where $A_i/A_{th} = 796$, $S_i = 0.4$.

According to nozzle geometry, drop growth in the convergent zone can be either significant (long convergent zone) or practically negligible (short convergent zone). It is to be noted, that the maximal saturation is reached in the nozzle throat, implying that the particles, that are not activated at the throat inlet, do not grow by condensation and they remain indetectable by optical system. *Fig. 4* shows that minimal activation diameter decreased according to the normalized section in the nozzle. Thus, to know the minimal diameter of the particles that will be activated in the nozzle, we must study the minimal diameter of activation in the nozzle throat.

Table 1 shows saturation variations reached in the nozzle throat in relation to relative humidity at the nozzle inlet and to downstream pressure. For downstream pressure of 600 hPa, the saturation in the nozzle throat always exceeds 2.4, corresponding to a minimal diameter of activated particles around 3 nm (*Table 2*). For relative humidity of 50%, the limit for critical saturation rate is exceeded, so in that case it is a risk to activate molecule aggregates and consequently to count more particle than there actually are. When the downstream pressure equals to 800 hPa, the saturation is still too low to activate particles with diameter under 10 nm (*Tables 1* and *2*) except at relative humidity of 50%. For downstream pressure of 700 hPa, the critical saturation ratio is never reached and particles with diameters of 10 nm are always activated for relative humidity values between 30 and 50%.

Table 1. Saturation in relation to downstream pressure (p) and relative humidity (H), and the critical saturation (S_c) in the nozzle throat (A_i / A_{th} = 44.4)

$H/p_{downstream}$ (%)	600 hPa	700 hPa	800 hPa
20	2.4	1.1	0.5
30	3.6	1.6	0.8
40	4.8	2.1	1.1
50	5.9	2.6	1.4
S_c	5.0	4.5	4.2

Table 2. Minimal activation diameter in relation to downstream pressure (p) and relative humidity (H)

$H/p_{downstream}$ (%)	600 hPa (nm)	700 hPa (nm)	800 hPa (nm)
20	3.0	40.5	-
30	2.0	5.3	-
40	1.6	3.3	24.4
50	-	2.5	7.5

Those effects are summed up in *Fig. 5*. The operating area of the system is included between the upper curve corresponding to (H_i, $p_{downstream}$), producing a critical saturation in the nozzle throat, and the lower curve represents the activation of particles with diameter of 10 nm in the nozzle throat.

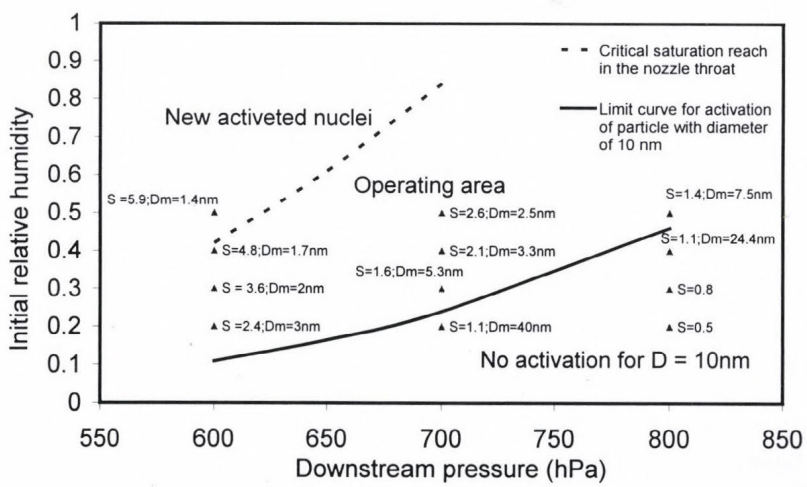

Fig. 5. Operating area of the system in relation to the downstream pressure and relative humidity at the nozzle inlet and downstream pressure (A_i / A_{th} = 44.4).

3.2 Particle growth in COPACHA

After the condensation process had been started, particles must grow in the nozzle until they reach an optically detectable diameter. Let us recall, that the minimal classically detectable diameter by optical particle counters is about 0.15 μm. In our system, since the particle growth occurs mainly in the nozzle throat, the retention time in the throat is an essential parameter. For initial droplet diameters between 10 nm and 100 nm, the relative velocity between the gas and the droplet increases in the first part of the nozzle and falls to zero in the throat. *Tables 3* and *4* indicate the final diameter of drops at nozzle outlet for different retention times and relative humidity values for aerosols with initial diameter of 10 nm.

Table 3. Final diameter of drops for different retention time (t_s, in ms) and relative humidity (H) values ($p_{downstream}$ = 700 hPa, D_i = 10 nm, A_i/A_{th} = 44.4)

H/t_s	**0.34**	**0.55**	**0.8**	**1**
%		**μm**		
30	0.06	0.10	0.14	0.17
40	0.11	0.18	0.25	0.30
50	0.16	0.25	0.34	0.41

Table 4. Final diameter of drops for different retention time (t_s, in ms) and relative humidity (H) values ($p_{downstream}$ = 600 hPa, D_i = 10 nm, A_i/A_{th} = 44.4)

H/t_s	**0.28**	**0.46**	**0.64**	**0.82**
%		**μm**		
20	0.06	0.09	0.12	0.15
30	0.10	0.16	0.21	0.26
40	0.15	0.22	0.29	0.36

Table 3 shows that for downstream pressure of 700 hPa and retention time exceeding 0.8 minutes, particles with an initial diameter of 10 nm grow sufficiently to be detected when the relative humidity remains within 30% and 50%. On the over hand, one can see from *Table 4* that for downstream pressure of 600 hPa and retention time of 0.82 minutes, the same particles grow sufficiently large to be detected when relative humidity is within 20% and 40%. *Table 5* gives the final size of drops in relation to the initial nucleus diameter. This table also shows that the influence of the initial diameter on the exit diameter is low. It is to be noted, that the effect of initial particle

concentration on saturation in the nozzle can be neglected for concentrations below 10^5 cm^{-3}. For higher particle concentration, the vapor content in the gas falls very quickly in the throat of the nozzle, which slows down the condensation on the droplet.

Table 5. Final diameter (D_f, in μm) of particles for different initial diameters (D_i) ($p_{downstream}$ = 700 hPa, H = 40%, t_s = 1 ms)

D_i	10 nm	20 nm	40 nm	60 nm	80 nm	100 nm
D_f	0.30	0.31	0.32	0.34	0.36	0.37

4. Conclusion

We have designed a new type of CNC that uses ambient humidity as working fluid. Our study indicates that COPACHA (Continuous Particle Counter by Condensation of Ambient Humidity) is able to detect particles with sizes larger than or equal to 10 nm for relative humidity values above 20%. It is also demonstrated that the operation downstream pressure must be between 600 and 750 hPa, and the minimal retention time at the nozzle throat must be about 0.8 minutes.

APPENDIX

The mean free path can be determined by the following equation (*Willeke,* 1986):

$$\lambda = \lambda_0 \left(\frac{\mu_{as}}{\mu_{as0}} \right) \left(\frac{p_0}{p} \right)^{\gamma} \sqrt{\frac{T_0}{T}},$$

where $\lambda_0 = 0.0653$ μm, $p_0 = 10^5$ Pa, $\mu_{as0} = 1.81 \times 10^{-5}$ Pa s, $T_0 = 293$ K.

The dynamic viscosity of air is calculated by the Sutherland's rule:

$$\mu_{as} = \mu_0 \sqrt{\frac{T}{T_0}} \frac{\left(1 + \frac{c}{T_0}\right)}{\left(1 + \frac{c}{T}\right)},$$

where $c = 123.6$ K, $\mu_0 = 171.1 \times 10^{-6}$ (Pa s), $T_0 = 273$ K.

Diffusion coefficient of water vapor in air (D_{vg}) is given by *Fuller et al.* (1966) as follows:

$$D_{AB} = \frac{10^{-3}\ T^{1.75}}{p\left(U_A^{1/3} + U_B^{1/3}\right)^2} \left(\frac{1}{M_A} + \frac{1}{M_B} \right)^{1/2},$$

where D_{AB} is given in $cm^2\ s^{-1}$, T in K, p in atm, while U values represent the atomic diffusion volumes given by *Fuller et al.* (1966). $U_{Air} = 20.1\ cm^3\ g^{-1}\ mol^{-1}$, $U_{water} = 9.44\ cm^3\ g^{-1}\ mol^{-1}$.

Sherwood and Nusselt numbers (*Hughmark,* 1967) can be tabulated as given below:

Re_d	Sc or Pr	Sh or Nu
$1 < Re_d < 450$	Sc or Pr < 250	Sh or Nu $= 2 + 0.6\ Re_d^{0.5}$ (Sc or Pr)$^{1/3}$
$1 < Re_d < 17$	Sc or Pr > 250	Sh or Nu $= 2 + 0.5\ Re_d^{0.5}$ (Sc or Pr)$^{0.42}$
$17 < Re_d < 450$	Sc or Pr > 250	Sh or Nu $= 2 + 0.4\ Re_d^{0.5}$ (Sc or Pr)$^{0.42}$

List of symbols

A	Nozzle surface at cross section x [m^2]
a	Sound velocity in fluid [$m\ s^{-1}$]
C_p	Specific heat at constant pressure
d	Nozzle diameter at cross section x [m]
D	Diameter of particles or drops [m]
D_{vg}	Vapor diffusion coefficient in gas [$m^2\ s^{-1}$]
H	Relative humidity
I	Nucleation rate [$m^{-3}\ s^{-1}$]
J	Mass flow of vapor onto a drop [$kg\ s^{-1}$]
k	Thermal conductivity of fluid [$W\ m^{-1}\ K^{-1}$]
K	Boltzmann's constant
Kn	Knudsen number
L	Latent heat [J kg]
l_{th}	Throat length [m]
l_{conv}	Convergent length [m]
M_{ach}	Mach number
M	Molecular weight [$kg\ mol^{-1}$]
m_v	Mass of a vapor molecule [$kg\ mol^{-1}$]
N	Particle concentration [m^{-3}]
Nu	Nusselt number for a sphere
p	Pressure [Pa]
Pr	Prandtl number
q	Total mass flux rate in the nozzle [$kg\ s^{-1}$]
Q_l	Condensation heat release [$J\ s^{-1}$]
Q_c	Conduction heat release [$J\ s^{-1}$]
r	Ideal gas constant [$J\ kg^{-1}\ K^{-1}$]
Re	Reynolds number
Re_d	Droplet Reynolds number
r_{gp}	Ideal gas constant [$J\ K^{-1}\ mol^{-1}$]
S	Saturation ratio
Sc	Schmidt number
Sh	Sherwood number
T	Temperature [K]
t_s	Retention time [s]
v	Fluid speed [$m\ s^{-1}$]
V	Average thermal velocity [$m\ s^{-1}$]
v_m	Molecule volume [m^3]
x	Abscissa in nozzle [m]
ρ	Density [$kg\ m^{-3}$]
γ	Ratio of gas specific heats
σ	Surface tension [$N\ m^{-1}$]
λ	Mean free path [m]
μ	Dynamic viscosity [Pa s]

Indices

as	Reference fact to dry air
a	Reference fact to aerosol
d	Reference fact to droplet
i	Reference fact to generator state

l	Reference fact to liquid phase
t	Reference fact to Knudsen regime
th	Reference fact to nozzle throat
v	Reference fact to vapor
vs	Reference fact to saturating vapor state
∞	Reference fact to state far from the droplet.

References

Ahn, K.H., 1988: Ultrafine aerosol measurement and particle activation and droplet growth processes in condensation nucleus counters. *Ph.D. Thesis*, University of Minnesota.

Barrett, J.C. and *Clement, C.F.*, 1986: A soluble one-dimensional problem for coupled heat conduction and mass diffusion with aerosol formation in a vapor-gas mixture. *J. Aerosol Sci. 17*, 129-143.

Devienne, M., 1958: *Frottement et échanges thermiques dans les gaz raréfiés*. Gauthier-Villars, Paris.

Fletcher, N.H., 1962: *The Physics of Rainclouds*. Cambridge University Press.

Fuchs, N.A., 1959: *Evaporation and Droplets Growth in Gaseous Media*. Pergamon, New York.

Fuchs, N.A. and *Sutugin, A.G.*,1970: *Highly Dispersed Aerosols*. Ann Arbor Science Publishers, Ann Arbor, Michigan.

Fuller, E.N., Schettler, P.D., and *Giddings, J.C.*, 1966: A new method for prediction of binary gas-phase diffusion coefficients. *Ind. Eng. Chem.*58, 19-26.

Götz, G, Mészáros, E., and *Vali, G.*, 1991: *Atmospheric Particles and Nuclei*. Akadémiai Kiadó, Budapest.

Hughmark, G.A.,1967: Mass and heat transfer from rigid spheres. *Am. Inst. Chem. Engng. J. 13*, 1219–1221.

Johnston, M.V. and *Wexler, A.S.*, 1995: Mass spectrometry of individual aerosol particles. *Analyt. Chem. 67*, 721A-726A.

Jurski, K. and *Gehin, E.*, 2003: Heterogeneous condensation process in an air water vapour expansion through a nozzle-experimental aspect. *Int. J. of Multiphase Flow 29*, 1137-1152.

Kurten, H., Raash, J., and *Rump, F.H.*, 1966: *Chem. Ing. Tech. 38*, 941-948.

Mallina, R.V. and *Wexler, A.S.*,1997: Particle growth in high speed particle beam inlets. *J. Aerosols Sci. 28*, 223-238.

McMurry, P.H., 2000: The history of Condensation Nucleus Counters. *Aerosol Sci. Technol. 33*, 297-322.

Renoux, A. and *Boulaud, D.*,1998: *Les aérosols, physique et métrologie*. Lavoisier ed, Paris.

Seinfeld, J.,H.,1986: *Atmospheric Chemistry and Physics of Air Pollution*. Wiley, New York.

Stodola, A.,1927: *Steam and Gas Turbines*. McGrawHill, New York.

Tom, J.W. and *Debenedetti, P.G.*, 1991: Particle formation with supercritical fluids. *J. Aerosol Sci.* 22, 555-584.

Turner, J.R., Kodas, T.T., and *Friedlander, S.K.*, 1988: Monodisperse particle production by vapor condensation in nozzles. *J. Chem. Phys. 88*, 457-465.

Willeke, K.,1986: Temperature dependence of particle slip in gaseous medium. *J. Aerosol Sci. 5*, 191-204.

Yang, J., Jaenicke, R., Dreiling V., and *Peter, T.*, 2000a: Rapid condensational growth of particles in the inlet of particle sizing instruments. *J. Aerosol Sci. 31*, 773-788.

Yang, J., Jaenicke, R., and *Dreiling, V.*, 2000b: A continuous nozzle CNC for CN and CCN counting. *J. Aerosol Sci. 31*, 809-810.

IDŐJÁRÁS

Quarterly Journal of the Hungarian Meteorological Service
Vol. 108, No. 2, April–June 2004, pp. 95–122

Application of a cloud model in simulation of atmospheric sulfate transport and redistribution Part II. Numerical experiments and discussion of results

Vlado Spiridonov[1] and **Mladjen Curic**[2]

[1]*Institute of Physics, Faculty of Natural Sciences and Mathematics, St. Cyril and Methodius University, Skopje, Macedonia; E-mail: vspiridonov@mol.net.mk*

[2]*Department of Meteorology, Faculty of Physics, University of Belgrade, Serbia E-mail: curic@ff.bg.ac.yu*

(Manuscript received September 25, 2002; in final form November 19, 2003)

Abstract—The simulation of the so called summer case with continental polluted field initialization has revealed that convective thunderstorm generates strong vertical transport of gases and particulate compounds from the planetary boundary layer (PBL) to the upper troposphere (UT), perturbation of physical and chemical properties of aerosol, modification of pollutant concentration, and change of the spatial distribution of chemical species. The early formation of precipitation and enhanced scavenging have contributed to formation of approximately 2.5 times greater equivalent air concentration of sulfate in precipitation near the surface, than that found in the air at this level. The key microphysical processes that transfer the dissolved matter to the resultant frozen hydrometeors are: the accretion of cloud water by snow, accretion of cloud ice by snow, depositional growth of snow, wet and dry growth of graupel, accretion of cloud water by graupel, and auto-conversion (aggregation) of snow.

The so called spring case numerical experiment with chemical background taken from Macedonia provided an insight into the potential influence on the long-range transport of atmospheric pollutants and ascertained quantitative-qualitative assessments about processes by which acidic species are incorporated into precipitation. The parameters computed by the model are in fairly good agreement with observations. The average equivalent cloud water pH and rainwater pH were about 5.0 and 4.5, respectively, when the most acidic precipitation occurred.

The results of the sensitivity tests of cloud chemistry to the physical processes in continental non-polluted and polluted environments indicate, that in-cloud nucleation and scavenging of aerosols account for 27% and 20% of the total sulfur mass removed by wet deposition in non-polluted and polluted cases, respectively. Sub-cloud scavenging contributes for about 35% and 29% of the total sulfur mass removed by wet deposition. Liquid-phase in-cloud oxidation contributes for about 35% and 32%, while

sub-cloud oxidation accounts for about 40% and 35% of the total sulfur mass deposited for non-polluted and polluted cases, respectively. Neglecting the ice phase when considering chemistry in continental non-polluted and polluted clouds may lead to overestimation by about 140% and 150% of the total sulfur mass removed by wet deposition. The assumption of Henry's law equilibrium for these types of clouds results in overestimation of about 148% and 133%, respectively.

Key-words: cloud modeling, chemical processes, microphysics, sulfate transport.

1. Introduction

Numerical experiments and model sensitivity tests have been performed utilizing a relatively sophisticated dynamical cloud model with simple sulfur chemistry (*Spiridonov* and *Curic*, 2003, hereafter referred as Part I). In Part II, we continue with examination of the dependence of the chemical fields upon the physical processes, which take place in the in-cloud and near-cloud environment. In this way, one can study the effects of deep convection on the redistribution of atmospheric pollutants and clarify some primary relationships among dynamical, microphysical, and chemical processes in three-dimensional space and complex cloud environment.

Here we present the results of the numerical experiments. Three-dimensional cloud chemistry simulations have been performed in order to understand the transport and transformations processes, and to investigate the modification of the sulfate concentration in the in-cloud and near-cloud environments. Two basic parameter sets have been used to initialize the cloud chemistry model.

2. Three-dimensional numerical experiments

In this section, mainly the microphysical and chemical parts of the results of numerical experiments, i.e., results of the solution of the equations formulated in Sections 2 and 3 of Part I are discussed. As it was mentioned, in order to understand the transport and redistribution processes of chemical species inside convective clouds and in the near-cloud environment, and to explore the changes of pollutant concentrations, three-dimensional simulations of the chemistry of such clouds have been performed. Of course, 3D runs are also important dynamically for studying the relationship between wind shear and veering, rotation and orientation of updrafts and downdrafts, cloud movement relative to the mean direction, and flow of environmental wind around the cloud.

2.1 Boundary conditions and numerical technique

Boundary conditions are specified along all sides of the integration domain, since the computations take place within a finite model domain. Along the bottom of the model domain the normal velocity w is set to zero. The open top boundary condition is applied in the model in order to eliminate strong internal gravity waves (*Klemp* and *Durran*, 1983). Also the normal second derivatives for the eddy mixing terms are set to be zero along the boundaries. This provides vertical gradients in the mean state so the profiles are not distorted due to eddy mixing near the boundaries. The lateral boundaries are open and time-dependent, so that disturbances can pass through with minimal reflection. Two different cases with regard to the wind velocity are considered, after *Durran* (1981). When the velocity component normal to the boundary is directed inside the domain (inflow boundary), normal derivatives are set to zero. At outflow boundaries, the normal velocity component is advected out through the boundary with an estimated propagation speed which is averaged in the vertical, and weighted at each level by the approximate local amplitude of the wave. Boundary conditions for the pressure are calculated from other boundary values to maintain consistency.

Model equations are solved on a standard spatially staggered grid. All velocity components, u_i are defined at one-half grid interval $0.5\,\Delta x_i$, while scalar variables are defined at the midpoint of each grid. The horizontal and vertical advection terms are calculated by centered fourth- and second-order differences, respectively.

Since the model equations are compressible, a time splitting procedure is applied to achieve numerical efficiency. With this procedure the sound wave terms are solved separately using a smaller time step, while all other processes are treated with a larger time step, Δt, which is appropriate to the time scales of physical interest. The small and large time steps are applied as follows. The scalar prognostic equations, except the pressure equation, are solved from $t-\Delta t$ to $t+\Delta t$ by a single leap-frog step. The terms which are not responsible for sound wave generation in the equations of motion and the pressure equation, are evaluated at the central time level t. Finally, the wind and pressure prognostic variables are stepped forward from $t-\Delta t$ to $t+\Delta t$, with forward time differencing by the small time step. In grid points adjacent to lateral boundaries, the normal horizontal advection terms are approximated using second-order differences instead of the fourth-order ones used elsewhere. At lateral boundaries, the normal derivatives for all prognostic variables are calculated with first-order accuracy, through one-sided differences lagged at time $t-\Delta t$ to provide stability.

2.2 Initial conditions and initialization procedure

Fig. 1 shows the representative radio-sounding for simulation of a moderate air mass thunderstorm which occurred on July 6, 1995. This is referred hereafter as summer case. The main characteristic of the sounding is a stable dry layer limiting cloud growth. The atmosphere was moist to the height of 350 hPa, with two thin layers of great thermal stability. The wind profile is characterized by weak wind velocity near the surface, veering at the sub-cloud layer, enhanced wind shear at the mid-level, and strong zonal wind at the upper levels. The initial mixing ratios of rain and solid water are set to zero at all levels. The initial values of the number concentration of cloud droplets, $N_1 = 1000$ cm^{-3}, and dispersion, $D_0 = 0.40$, used in this study for the computation of auto-conversion are consistent with the nature of continental clouds.

Table 1 lists the chemical field initialization used to simulate two environments: (i) continental non-polluted background and (ii) continental polluted one.

The initial fields of temperature, humidity, horizontal wind velocity, and chemical data giving the input for the April 3, 2000 case (spring case) are depicted in *Fig. 2*. The concentrations of SO_2, H_2O_2, O_3, and NH_4^+ and SO_4^{2-} aerosols are assumed to fall exponentially with height, e.g.,

$$q_i(z) = q_i(0)\mathrm{e}^{-z/H}, \tag{1}$$

where $q_i(0)$ is the mixing ratio of component i at the lowest model level; H is the model scale height.

Initial impulse for convection is an ellipsoidal warm bubble of the form

$$\Delta T = \Delta T_0 \cos^2 \frac{\pi}{2}\beta \qquad \text{for} \quad \beta < 1, \tag{2}$$

where

$$\beta = \left[\left(\frac{x - x_c}{x_*}\right)^2 + \left(\frac{y - y_c}{y_*}\right)^2 + \left(\frac{z - z_c}{z_*}\right)^2\right]^{1/2}. \tag{3}$$

Here, the subscript c refers to the location of the center of the perturbation, while x_*, y_*, z_* are radial dimensions of the bubble. Values used for these simulations are $x_c = 12$ km, $y_c = 6$ km, $z_c = 0.5$ km, $x_* = y_* = 2.8$ km, $z_* = 0.5$ km, and the temperature perturbation is maximum in the bubble center, distinguishing $T_0 = 4$°C for the summer case simulation and $T_0 = 3.6$°C for the spring case, and exponentially decreasing to zero on the bubble boundary.

The initial perturbation of water vapor mixing ratio, caused by this initial temperature perturbation, is calculated with assumption that relative humidity has the same value as it had before the perturbation.

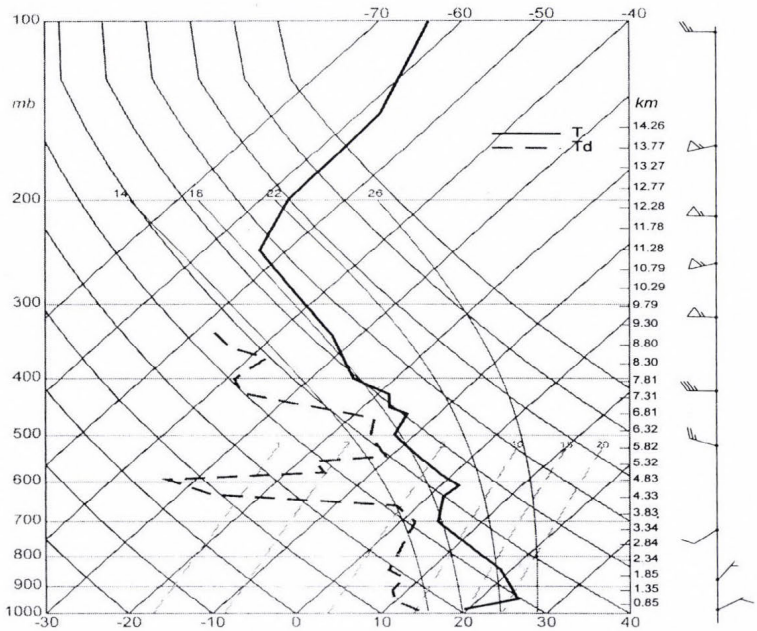

Fig. 1. The 00:00 UTC atmospheric sounding for Skopje, on July 6, 1995. Coordinate lines denote pressure (hPa) and temperature (°C). The solid line represents the temperature profile and the dashed line represents the moisture profile. Symbols on the right side of the same figure denote wind profile (direction and velocity).

Table 1. Initial fields of chemical species involved in sulfate production, for continental non-polluted and continental polluted background, based on *Taylor* (1989b)

Chemical species expressed through mixing ratios	$q_i(0)$ [μg kg^{-1}(air)]		H (km)
	Continental non-polluted clouds	Continental polluted clouds	
q_{SO_2}	4.42	21.0	2.0
$q_{SO_4^{2-}}$	3.1	16.0	3.5
$q_{NH_4^+}$	0.58	3.0	3.5
$q_{H_2O_2}$	0.59	0.59	-
q_{O_3}	82.8	82.2	-

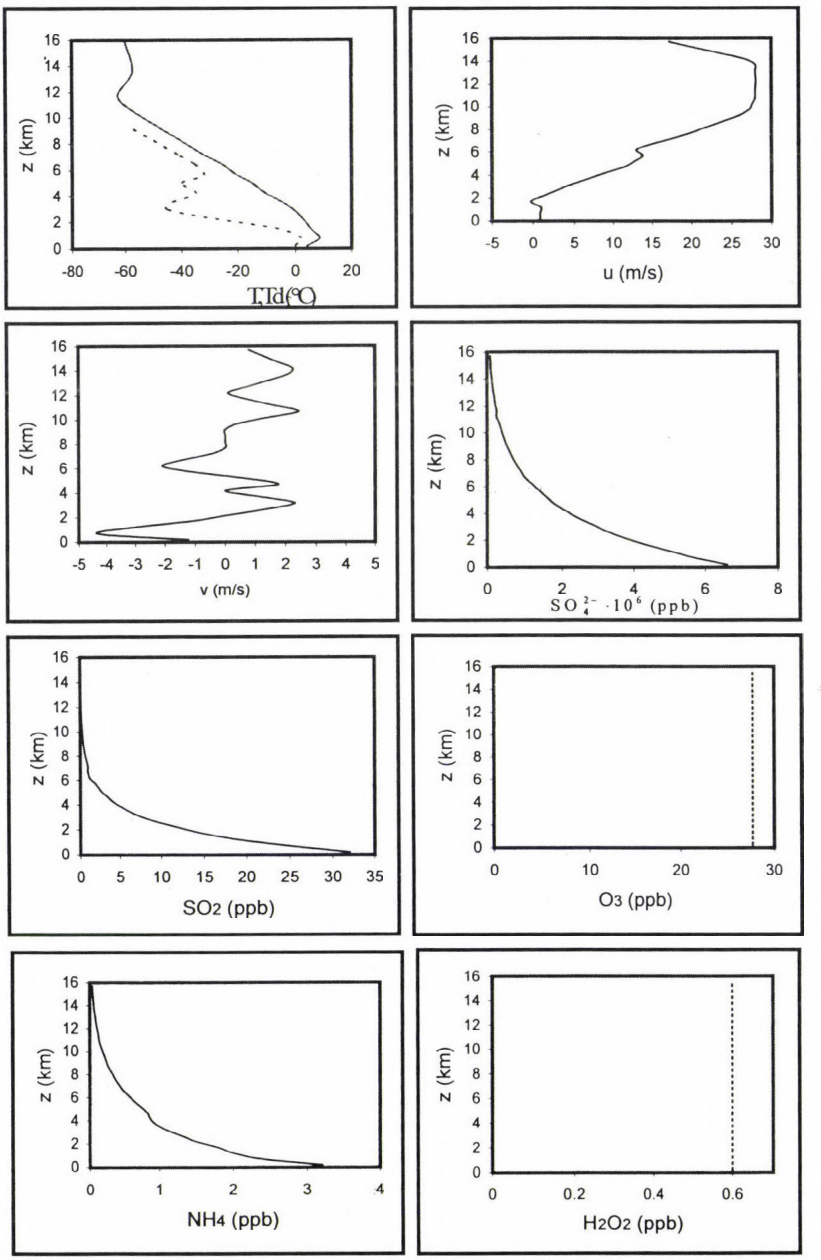

Fig. 2. The initial fields of temperature, humidity, u and v the horizontal wind velocity components and the chemical data set input of SO_4^{2-}, SO_2, O_3, NH_4^+, and H_2O_2 (in ppb), for April 3, 2000.

The model domain for the summer case simulation is 45 km × 45 km × 15 km. The model for the spring case is configured to a 24 km × 24 km × 12 km domain. The horizontal resolution of the model is 1 km, while the vertical one is 0.25 km for the summer case and 0.5 for the spring case run. The temporal resolution of the model is 5 and 10 s for integration of the dynamics, microphysics, and chemistry, and a smaller one is 0.2 and 2 s for solving the sound waves. The same temporal resolution is taken for solving aqueous phase chemistry and transport of chemical species.

3. Results

A number of case studies have been performed in the past to verify and document the value of the present cloud model in contributing to the understanding of convective storm dynamics and microphysics (e.g., *Telenta* and *Aleksic*, 1988; *Curic et al.*, 1999; *Spiridonov* and *Telenta*, 2000).

3.1 The summer case simulation of July 6, 1995

Numerical simulation results shown in *Fig. 3* indicate development of the model cloud starting at time 12.5 min. after initialization. Strong updrafts rapidly move the cloud towards the super-cooled zone, forming traces of ice crystals. After 23 min. the simulated cloud could be described as Cu med. with cloud water mixing ratio 7.5 g kg^{-1} and two minutes later raindrops occur with mixing ratio of 0.3 g kg^{-1}. Hail occurs in the 28th min and snow in the 29th, when the cloud could be identified as Cu cong. with depth about 9.6 km. Soon after that massive formation of graupel gives the intensive vertical development of the cloud an important energy source. In 40 minutes simulation time, hail reaches its maximum mixing ratio 16.0 g kg^{-1}. In 45 minutes the cloud top penetrates the tropopause, soon after that our 3D run indicates rapid transformation of graupel to rain, while the melting graupel also enhances precipitation, and the mixing ratio of rain increases to its maximum value of 12.7 g kg^{-1}. The mature stage of the simulated storm comes after 70 min. of integration when extensive precipitation occurs. The fallout of hydrometeors weakens the updraft intensity and cuts off the supply of moisture from the surface, so the cloud top spreads horizontally forming the characteristic anvil. The weakened surface convergence indicates the entering of dissipation stage, although, remaining anvil survives for a much longer time. After 120 minutes, only fragmented structure of the cloud remains in the integration domain. The maximum accumulated rain is 175 mm, and accumulated hail is 1.3 kg m^{-2}. In summary, the three-dimensional simulation indicates a moderate air mass thunderstorm with appearance of large amount of precipitation.

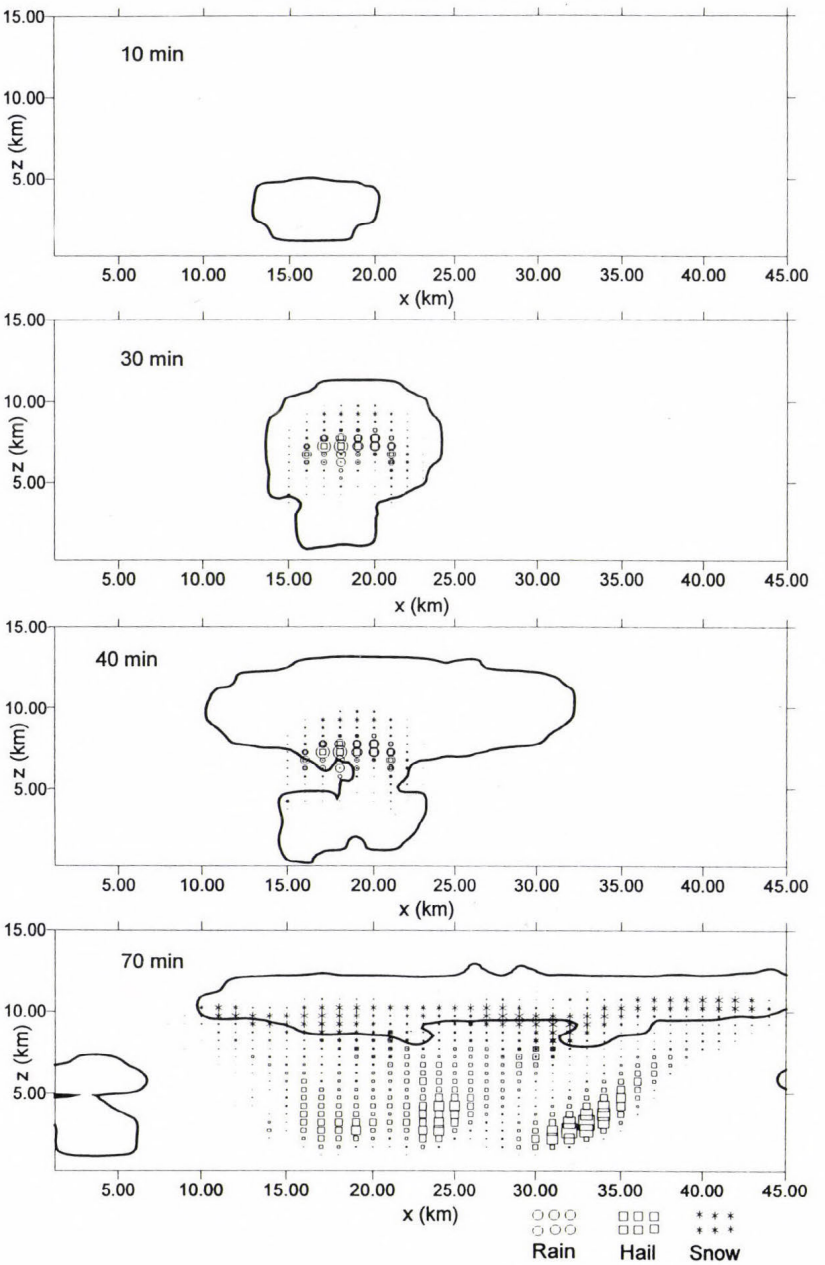

Fig. 3. General cloud appearance at 10, 30, 40, and 70 min. in $x - z$ plane at $y = 8.0$ km. Cloudy areas are outlined by the solid line with cloud water mixing ratio = 0.01 g kg^{-1}. Dots and rectangular boxes indicate rain and hail mixing ratios greater than 0.5 g kg^{-1}, respectively. The asterisks denote the snow mixing ratio greater than 0.5 g kg^{-1}.

The real microphysical structure of the storm chosen for numerical simulation was examined through calculations of the maximum radar reflectivity factor. The time evolution of the radar reflectivity maps are shown in *Fig. 4*. Dominant features are the temperature perturbation and appearance of the first radar echo 12 min. after the initialization. Then one can note rapid growth and spread of the radar reflectivity in the super-cooled zone of the cloud model domain. This phase of cloud evolution is characterized by intensive microphysical transformations. The formation of precipitation is evident on the radar reflectivity patterns from 30 to 50 min., when maximum radar reflectivity is found in the warm sector of the model domain. *Table 2* shows the comparison between some simulated and observed parameters for the analyzed case.

Vertical cross-sections of the integrated SO_4^{2-} aerosol mixing ratio in the simulated storm built up in 10, 30, 40, and 50 minutes are presented in *Fig. 5*. A three-dimensional view of sulfate transport and redistribution inside the convective cloud volume is shown in *Fig. 6*. It is conspicuous that sulfate transport and changes of its spatial distribution go parallel with cloud formation and evolution. Convergence near the cloud base is the result of mass transfer by nucleation scavenging and Brownian diffusion. The formation of rain leads to a more uniform distribution of aerosol mass. After this, the updrafts are no longer sufficient to maintain the mass flux, and scavenging by rain successively reduces the mass of cloud-dissolved sulfate. The equivalent air concentration of sulfate in the precipitation near to the surface is approximately 2.5 times higher than the concentration in the air at this level. It suggests that both processes, oxidation by O_3 and H_2O_2 in rainwater and scavenging by rain, contribute to the formation of excess sulfate near to the surface. We found that after 40 min. simulation time, sulfate reaches the ground leading to wet deposition. Small portion of sulfate mass, which is not scavenged by hydrometeors, is advected by flows at upper cloud levels led by the basic tropospheric wind. As time elapses, evaporation from precipitation becomes so important, that a fraction of the sulfate is transferred back into the air.

Evolution of the pH factor in cloud water and rainwater after 20, 30, 40, and 50 min. of simulation time is shown in *Fig. 7a,b*. The dashed curves delineate the cloud and rainwater boundary, while solid lines display the pH factor distribution in cloud and rainwater, respectively. The strong gradient of cloud water acidity in early stages of cloud development is due to mass convergence and dissolution of pollutants in cloud water close to the central part of the cloud. In the mature stage, successive weakening of the gradient followed by slight lowering of cloud water acidity can be seen. Subsequently, the formation of precipitation induces rain scavenging and dissolution of pollutants, contributing to much more uniform pH distribution. The average

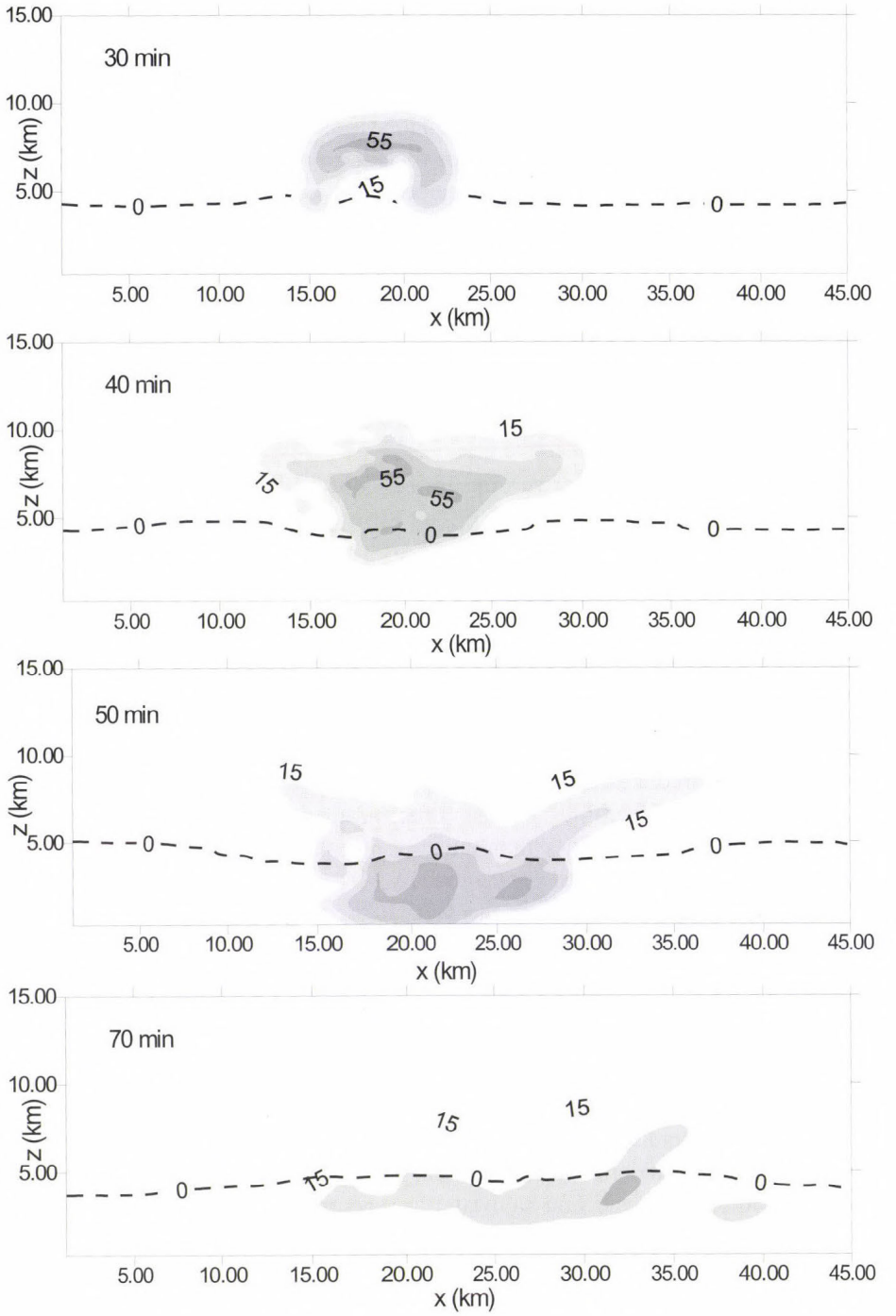

Fig. 4. The radar reflectivity history maps (dBz) in $x - z$ plane at $y = 8.0$ km at 30, 40, 50, and 70 min. Dashed lines denote distribution of 0°C isotherm.

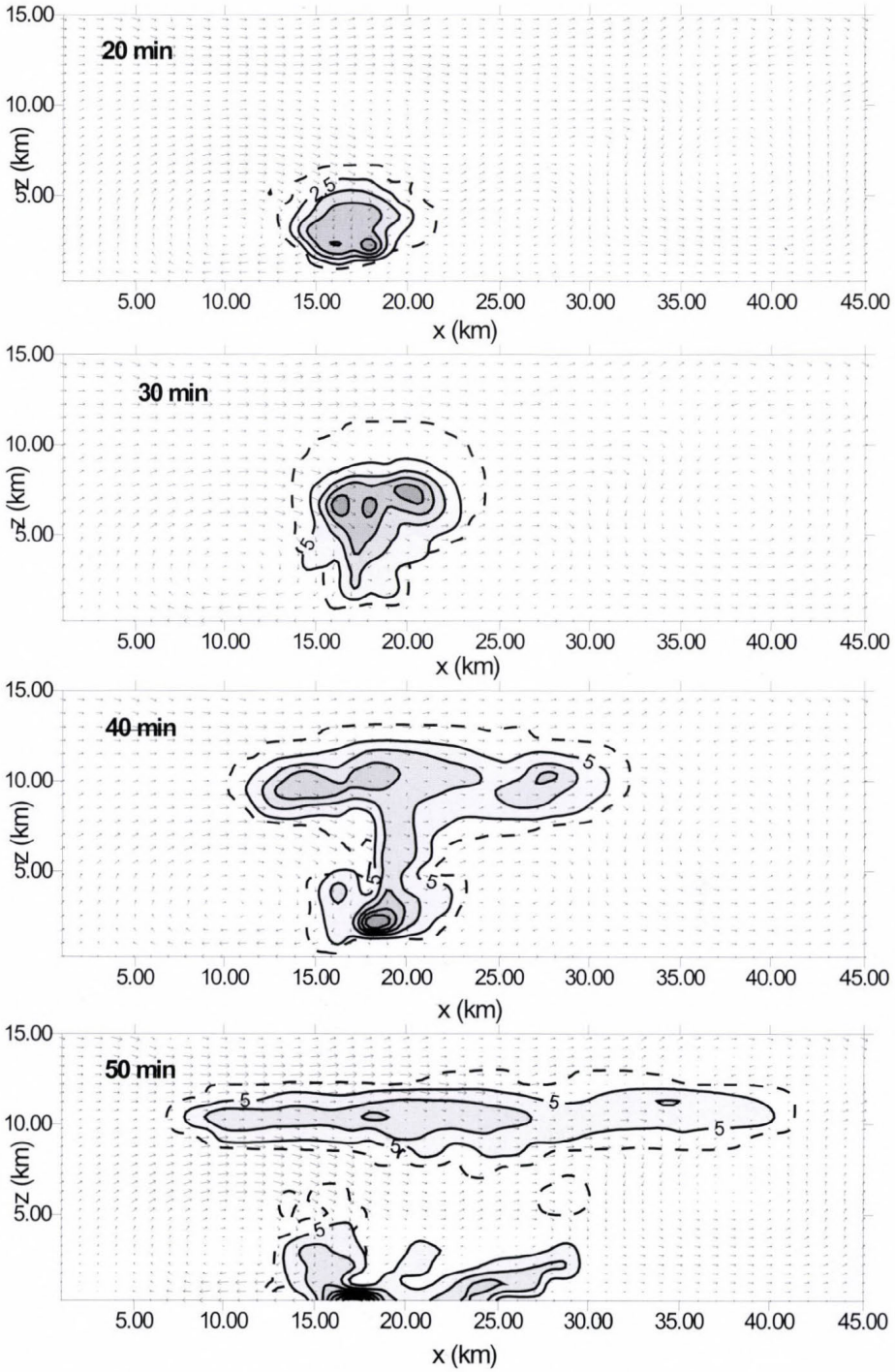

Fig. 5. Time evolution of sulfate concentration in the cloud (μg m^{-3}) in $x - z$ plane at $y = 8.0$ km in 10, 30, 40, and 50 min. of the simulated storm on July 6, 1995. Arrows denote wind fields.

Table 2. The comparison between simulated and observed parameters on July 6, 1995 (summer case)

Parameter	Cloud base (km)	Cloud top (km)	Max. vertical velocity ($m\ s^{-1}$)	Max. radar reflectivity (dBz)	Total acc. rain ($kg\ m^{-2}$)	Total acc. hail ($kg\ m^{-2}$)
Model	2.2	13.5	20.4	56	175	1.3
Observed	2.4	14.6	18.3	50	180	-

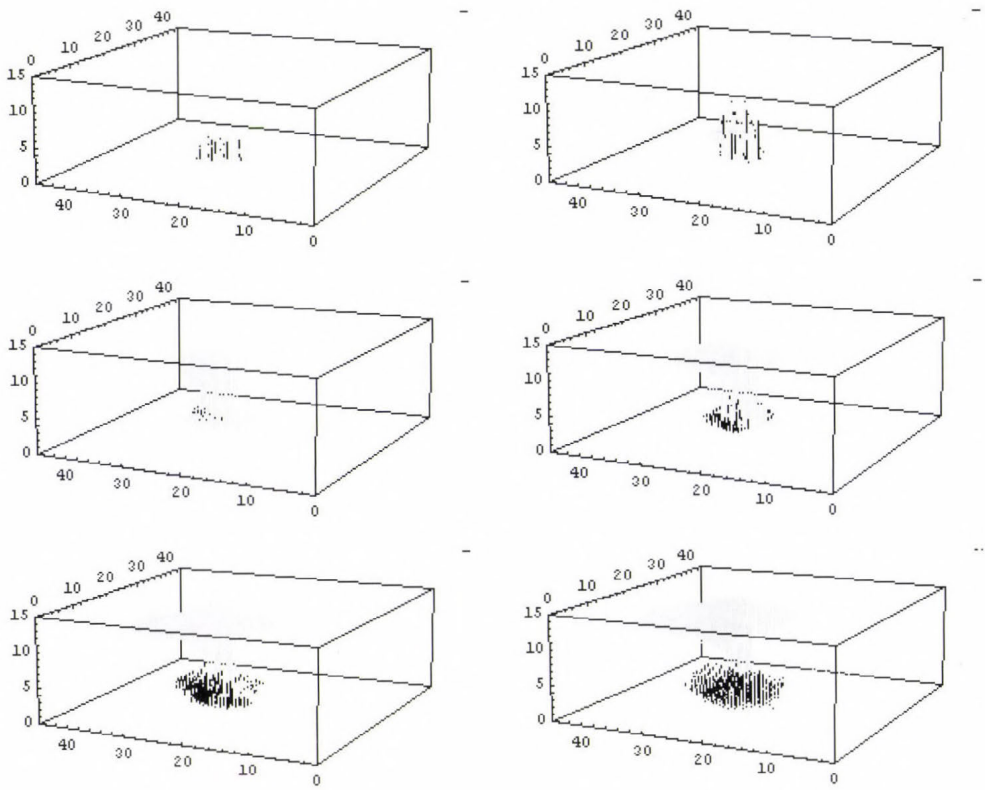

Fig. 6. Three-dimensional view of sulfate transport and redistribution, in 10, 20, 30, 40, 50, and 120 min. of time. The dark patterns delineate cloud water mixing ratio greater than 0.01 g kg^{-1}, the light fields are sulfate concentrations greater than 2.5 ($\mu g\ m^{-3}$).

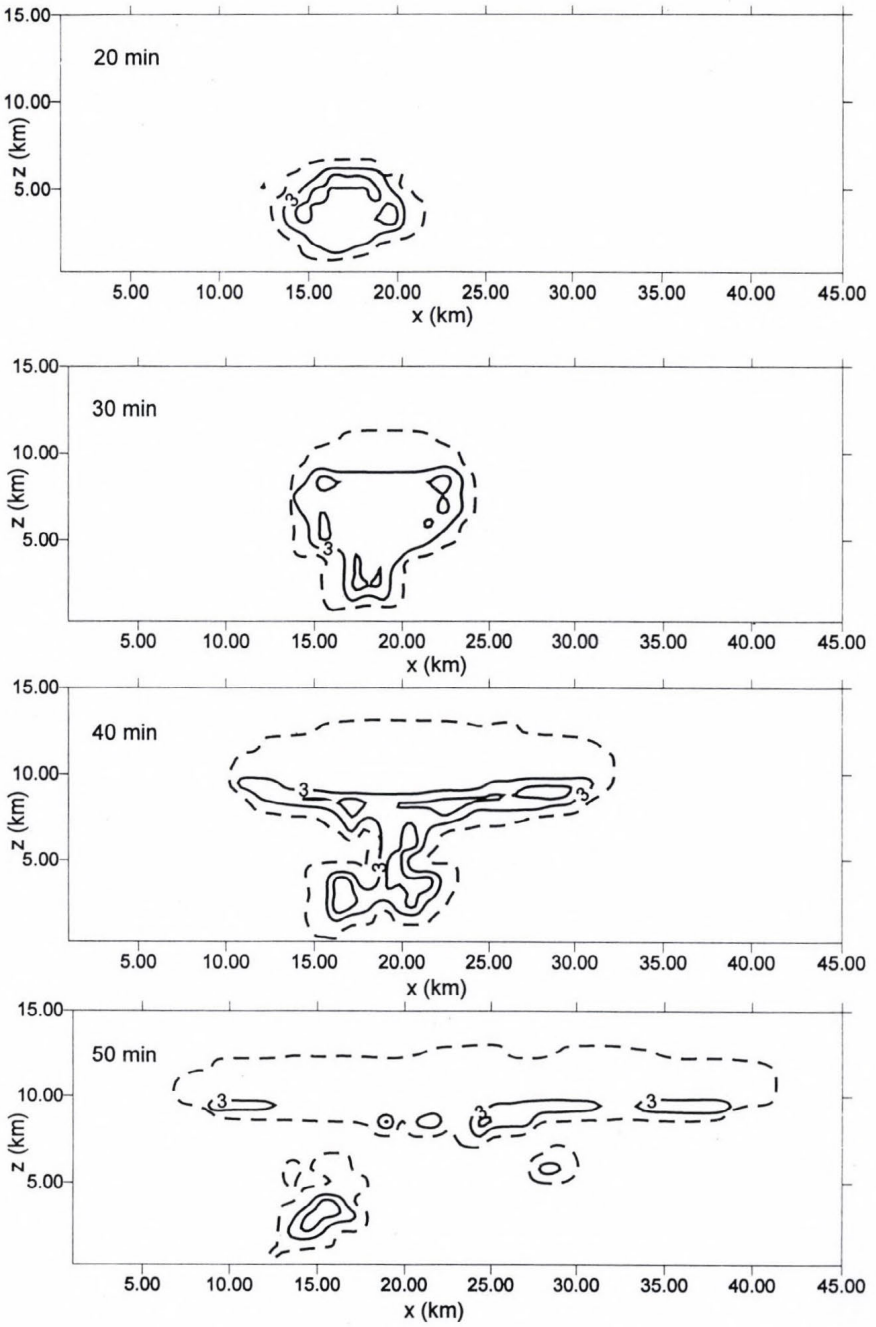

Fig. 7a. Time evolution of the pH values of cloud water in the $x-z$ plane at $y = 8.0$ km, in 20, 30, 40, and 50 min. of the simulation time.

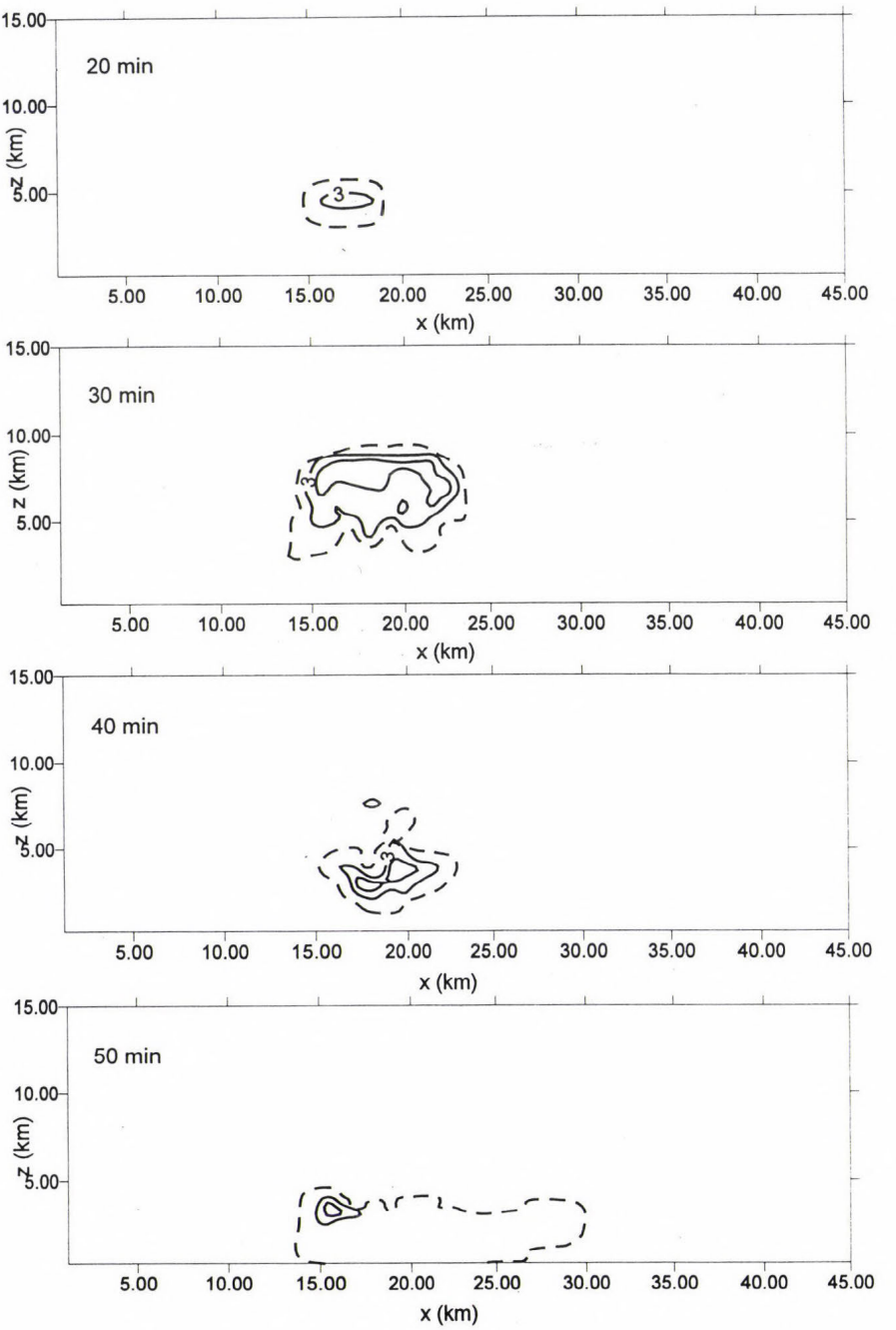

Fig. 7b. Time evolution of the pH values of rainwater in the x–z plane at $y = 8.0$ km, in 20, 30, 40, and 50 min. of the simulation time.

pH of rain near the ground is lower than 3.0 demonstrating the influence of increased nucleation and oxidation on the acidity of the rain. Similar results for the pH distribution, but for warm clouds are illustrated in the study by *Tremblay* and *Leighton* (1986) and for a one-dimensional case by *Taylor* (1989b). The higher pH in *Taylor* (1989b) is a result of the assumed Henry's law equilibrium and implicit treatment of gases taking part in sulfate production. The lower calculated rainwater pH in *Tremblay* and *Leighton* (1986) is mainly due to the cloud model limitation, the warm cumulus convection ignoring ice-phase processes.

3.2 The spring case simulation of April 3, 2000

Large amount of mineral dust can be mobilized over the Sahara and injected into the atmosphere under favorable atmospheric conditions. Even areas far away from the desert such as Macedonia are sometimes affected by dust transport and deposition, when dust behaves as a pollutant that significantly reduces the air quality. It also causes the increase of content of all chemical components, both anions, cations, and heavy metals (*Nickovic et al.*, 2000). Ambient SO_4^{2-} aerosol concentrations during such dust storms may considerably exceed international standards for allowable concentrations.

In order to understand the sulfate aerosol transport and transformation processes in such conditions and to investigate the modification of pollutant concentration in the local cloud environment, also fully three-dimensional simulation of the chemistry of a convective cloud have been performed.

The time evolution of the size-integrated SO_4^{2-} aerosol concentration distribution during the storm's life is depicted in *Fig. 8.* The numerical simulation has shown rapid vertical transport of sulfate in the cloud formation stage due to the mass transfer by nucleation of the sulfate particle matter. Subsequently, this cloud parcel is advected and dispersed by the turbulent flow field. Enhanced zonal flows at the upper level rapidly move the polluted cloud into the central part of the integration domain. Early formation of rain contributes to enhanced microphysical sulfate mass exchange among different water species. The much higher sulfate concentration value after 30 min. is mainly due to oxidation of SO_2 to SO_4^{2-} and scavenging processes. After this the updrafts are not sufficient to maintain sulfate mass at the cloud base, and washout by rain gradually reduces cloud dissolved sulfate. It is also seen, that rain-laden sulfate reaches the ground after 30 min., causing wet deposition at the surface. The short time cycle of the convective cloud does not allow continuation of the process, and cloud enters into dissipative stage.

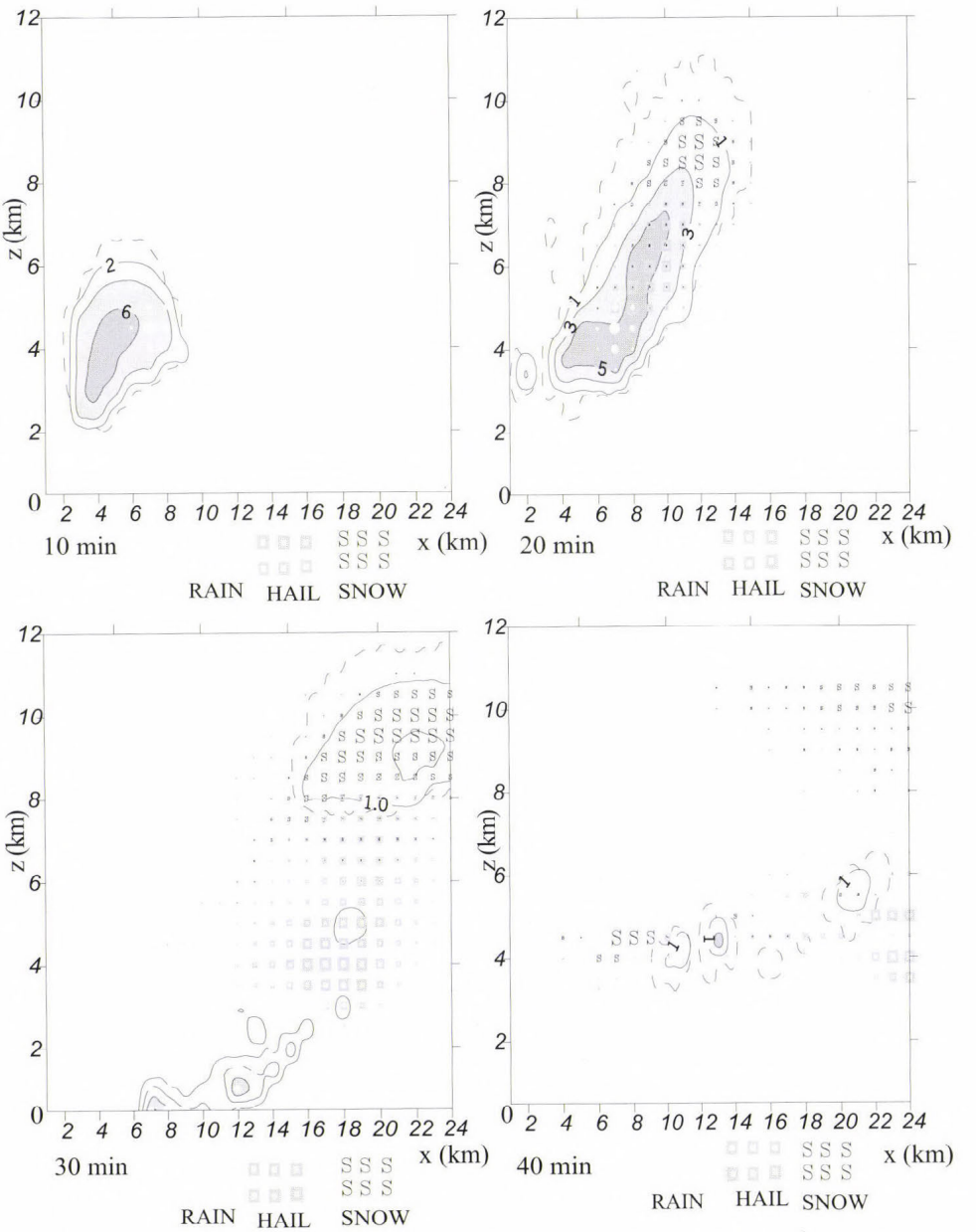

Fig. 8. Time evolution of sulfate (SO_4^{2-}) aerosol concentration (mg ℓ^{-1}) in 10, 20, 30, and 40 min., in the simulated cloud, in the x–z plane at $y=10$ km, on April 3, 2000. Cloudy areas are outlined by the dashed line with (cloud water + cloud ice) mixing ratio greater than 0.01 g kg^{-1}. Dots and asterisks indicate rain and hail mixing ratios greater than 0.5 g kg^{-1}, respectively. The symbol '*s*' denotes the snow mixing ratio greater than 0.5 g kg^{-1}. The solid curves represent isopleths of SO_4^{2-} fields in the simulated cloud.

Table 3 lists some parameters that characterized the numerical simulation performed here. Among others, maximum volume concentration of SO_4^{2-} (mg ℓ^{-1}), pH of cloud and rainwater, respectively, and total wet deposition (mg m^{-2}) for 60 min simulation were calculated.

Table 3. List of the model calculated parameters for the spring case simulation

Parameter	Time (minute)					
	10	**20**	**30**	**40**	**50**	**60**
Total rainfall (ℓ m^{-2})	0.0	0.0	5.6	19.5	24.3	27.8
pH – cloud water	5.0	6.0	6.5	6.0	5.0	5.5
pH – rain	3.0	4.5	7.0	3.6	4.5	5.5
Max. concentration $[SO_4^{2-} - S]$ (μg m^{-3})	4.3	6.5	8.0	10.5	8.0	5.5
Total wet deposition $[SO_4^{2-} - S]$ (mg m^{-2})	0.0	0.2	15.4	29.4	38.4	40.2
Max. ionic concentration $[NH_4^+]$ (μg m^{-3})	0.6	0.6	0.6	0.6	0.5	0.4
Mixing ratio of rain, q_R (g kg^{-1})	0.0	0.1	0.4	0.4	0.4	0.4
Mixing ratio of snow, q_S (g kg^{-1})	0.0	0.6	1.5	1.5	1.5	1.5
Max. vertical velocity, W_{max} (m s^{-1})	11.6	12.8	13.9	13.9	13.9	13.9

3.3 Comparison between simulated and measured of cloud chemical characteristics

Model results were compared to those observed and analyzed by standard laboratory methods. Precipitation samples from meteorological station Lazaropole (located in a rural representative area at 1333 meters a.s.l.) have been collected in every 24 hours with a wet only sampler ARS 1510. These measurements are continuously carried out in the framework of the European Monitoring and Evaluation Programme (EMEP). The chemical analysis of rainfall samples is performed using standard methods for anions (see, e.g., *Nickovic et al.*, 2000; *Andreevska et al.*, 2001).

The observed and measured parameters detected in precipitation samples for the period March–April 2000 are listed in *Table 4*. It is conspicuous, that

maximum amount of rainfall, pH, volume concentration of SO_4^{2-}, and wet deposition have really occurred on April 3 and 4. It is certain, that unstable conditions and convection contributed to the maximum rainfall and adequately higher concentration and deposition values in that period.

Table 4. Rainfall, pH, sulfate volume concentration and wet deposition, measured at the meteorological station Lazaropole during March–April, 2000

Date	Rain (ℓ m^{-2})	pH	SO_4–S (mg ℓ^{-1})	SO_4–S (mg m^{-2})
March 2–3, 2000	19.0	4.75	0.107	2.04
March 5–6, 2000	0.8	4.46	0.371	0.287
March 15–16, 2000	25.2	4.47	0.107	2.70
March 16–17, 2000	1.4	5.38		
March 17–18,2000	0.2	4.99		
March 18–19, 2000	0.1	4.53	0.270	0.027
March 26–27, 2000	1.7	5.36	0.964	1.64
March 27–28, 2000	8.1	5.05	0.321	2.60
April 1–2, 2000	6.2	6.10	1.070	6.63
April 3–4, 2000	**30.2**	**7.65**	**6.690**	**42.04**
April 4–5, 2000	**6.0**	**7.78**	**3.540**	**21.22**
April 5–6, 2000	6.1	6.26	0.910	5.54
April 6–7, 2000	2.7	4.70	0.320	0.87
April 7–8, 2000	2.4	5.68		
April 10–11, 2000	11.3	5.52	3.620	7.97
April 18–19, 2000	2.2	6.43		
April 19–20, 2000	2.6	6.04	0	0
April 20–21, 2000	4.0	4.11		
April 25–26, 2000	9.0	4.28	0.129	1.16
April 29–30, 2000	5.0	4.10	0.740	3.70
April 30–May 01, 2000	8.2	4.07	0.160	1.31

Note: On April 3 and 4, unstable conditions and strong convection led to the high concentration and deposition values.

The comparative analysis has shown good agreement between simulated and observed total accumulated precipitation. Higher measured pH values as compared to calculated pH = 5.5 are probably due to the fact, that dust is an alkaline compound that increases the pH value. There is also a fairly good agreement between measured and calculated total wet deposition of SO_4^{2-}. The latter was 40.16 mg m^{-2} for 120 min. simulation time. One of the reasons for higher simulated concentration value of SO_4^{2-} (10.50 mg ℓ^{-1}) is the result of using higher initial SO_4^{2-} concentration. The laboratory results and peaks have also shown good coincidence with the model-computed results.

These results have also been compared with the results of chemical analysis of precipitation at the main meteorological station (MMS) Lazaropole taken from the study on air pollution monitoring system in FYROM, published by the Japan International Cooperation Agency (*JICA*, 1999). Results shown in *Table 3* show quite reasonable values of pH in comparison to annual averaged pH value (6.22). There is also good agreement between calculated and measured SO_4^{2-} and NH_4^+ ionic concentrations.

Table 5. The relative contribution of the total sulfur and NH_4^+ mass removed by wet deposition for continental non-polluted and continental polluted background for a summer case simulation on July 6, 1995. The asterisk represents which chemical or physical parameterization is not involved in the simulation

3D Model run	Absorption		Nucleation and impact scavenging		Liquid-phase oxidation of SO_2 by H_2O_2 and O_3		Aqueous simulation of ice phase	Sulfur and NH_4^+ integrated precipitation mass (in kg)			
	Kinetic/Henry's Law		in-cloud/subcloud		in-cloud/subcloud			Continental clouds non-polluted / polluted			
								SO_4^{2-}	NH_4^+	SO_4^{2-}	NH_4^+
I	yes*	no	yes	yes	yes	yes	yes	8.12	3.42	26.20	6.84
II	no	yes*	yes	yes	yes	yes	yes	12.05	4.43	42.17	12.50
III	yes	no	no*	yes	yes	yes	yes	5.93	2.39	20.75	5.52
IV	yes	no	yes	no*	yes	yes	yes	5.20	2.00	17.51	5.06
V	yes	no	yes	yes	no*	yes	yes	5.05	3.42	16.95	6.84
VI	yes	no	yes	yes	yes	no*	yes	4.75	3.42	16.70	6.84
VII	yes	no	yes	yes	no*	yes	no*	11.30	4.78	39.79	11.43

4. The model sensitivity tests

The relative importance of absorption, scavenging, oxidation, and ice phase processes in the production and subsequent deposition of SO_4^{2-}, for mid-latitude moderate air mass thunderstorms have been determined from the cloud model generated microphysics and chemical fields. *Table 5* gives the parameters that distinguish among the seven numerical experiments carried out here. The first run that includes entire chemistry serves as a basis for comparison to each other. *Table 6* lists the sulfate source terms for the summer case simulation on July 6, 1995. As it can be seen from *Table 6*, the dominant production terms that control the sulfate chemical reactions are the SO_4^{2-} nucleation scavenging (PS3), oxidation of S(IV) in cloud water and rainwater by O_3 and H_2O_2 (PS2, PS9), SO_4^{2-} transfer from cloud water to cloud ice as

a result of depositional growth of cloud ice (PS14), and transfer of cloud water to SO_4^{2-} when cloud droplets evaporate (PS15).

Table 6. The sulfate production terms for the summer case simulation on July 6, 1995 (kg $kg^{-1}s^{-1}$). All terms are defined in Part I. Symbols in bold letter denote the dominant sulfate source terms

PSU1	$0.3 \cdot 10^{-12}$	**PSU2**	$0.1 \cdot 10^{-8}$	**PSU3**	$0.3 \cdot 10^{-9}$	PSU4	$0.1 \cdot 10^{-12}$	PSU5	$0.9 \cdot 10^{-11}$
PSU6	$0.4 \cdot 10^{-13}$	PSU7	$0.4 \cdot 10^{-11}$	PSU8	$0.9 \cdot 10^{-12}$	**PSU9**	$0.8 \cdot 10^{-8}$	PSU10	$-0.2 \cdot 10^{11}$
PSU11	$0.3 \cdot 10^{-11}$	PSU12	$0.2 \cdot 10^{-11}$	PSU13	$0.2 \cdot 10^{-11}$	**PSU14**	$0.3 \cdot 10^{-10}$	**PSU15**	$0.5 \cdot 10^{-10}$
PSU16	$0.7 \cdot 10^{-12}$	PSU17	$0.1 \cdot 10^{-11}$	PSU18	$-0.7 \cdot 10^{18}$	PSU19	$0.6 \cdot 10^{-19}$	PSU20	$0.2 \cdot 10^{-11}$
PSU21	$0.2 \cdot 10^{-12}$	PSU22	$0.3 \cdot 10^{-12}$	PSU23	$0.1 \cdot 10^{-13}$	PSU24	$0.2 \cdot 10^{-14}$	PSU25	$0.2 \cdot 10^{-12}$
PSU26	$0.5 \cdot 10^{-11}$								

4.1 The absorption of chemical species

The absorption of gas phase chemical species into cloud water and rainwater is determined by either Henry's law equilibrium or by explicit time-dependant calculation of gas transfer to droplets, using mass transfer limitation calculations.

Fig. 9a shows how the mixing ratios of gases included in sulfate production, dissolved in the cloud water and rainwater, are propagated and distributed within the simulated storm by applying the kinetic gas uptake method. Panels shown in *Fig. 9b* depict distributions of gases assuming Henry's law equilibrium. The difference is more emphasized for a more soluble gas as hydrogen peroxide.

The assumption of Henry's law equilibrium leads to about 148% higher value of the integrated sulfate mass removed by wet deposition for continental non-polluted clouds, and about 133% for continental polluted clouds. It suggests that models of mid-latitude continental storms, which neglect kinetic gas uptake limitations, will tend to over-predict the wet deposition.

4.2 The effects of in-cloud and sub-cloud scavenging for continental non-polluted and polluted clouds

Scavenging is found to be a very important process contributing to the redistribution of sulfate, which can cause decrease of concentrations of chemical species inside the cloud and in the near-to-cloud environment. The efficiency of scavenging processes in the production and subsequent deposition

of SO_4^{2-} for the continental non-polluted and polluted air mass thunderstorms were determined from the model generated microphysical and chemical fields.

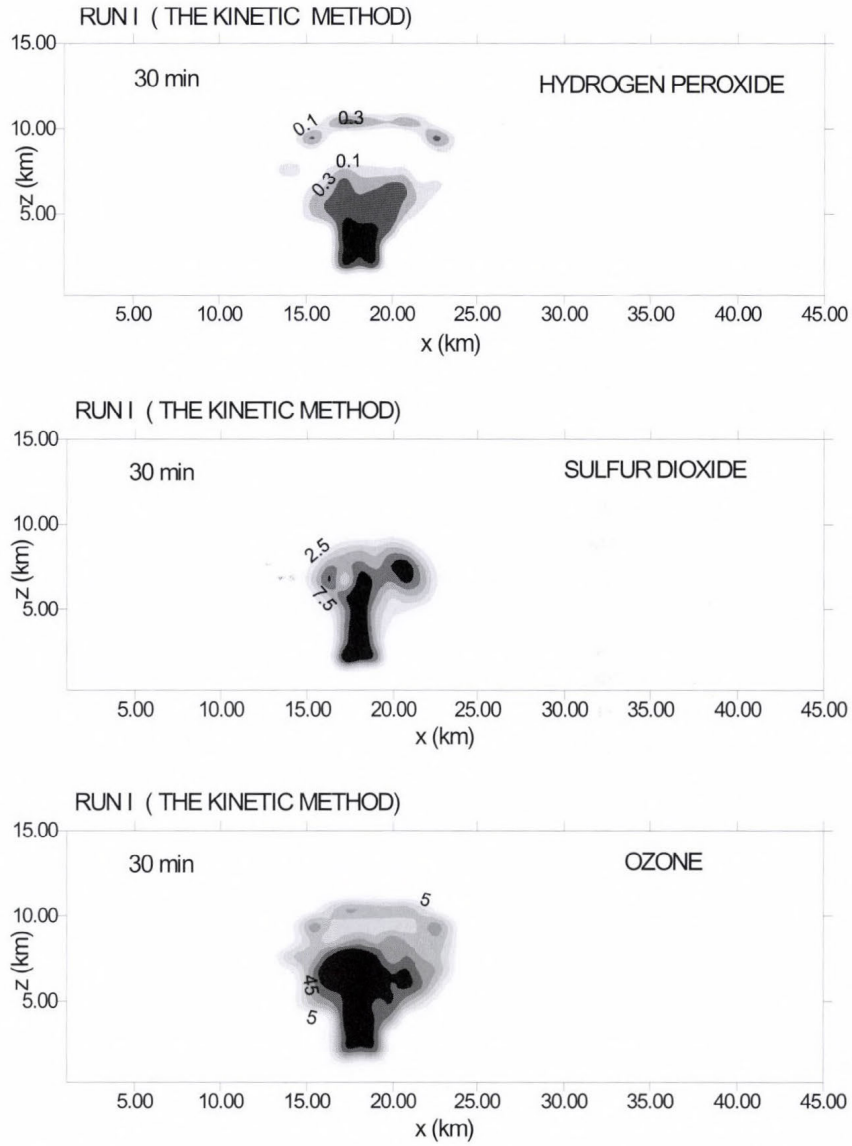

Fig. 9a. Time evolution of H_2O_2, SO_2, and O_3 concentrations in ($\mu g\ m^{-3}$) in x–z plane at $y = 8$ km, in 30 min. of the simulated cloud on July 6, 1995, by including method of kinetic gas limitations.

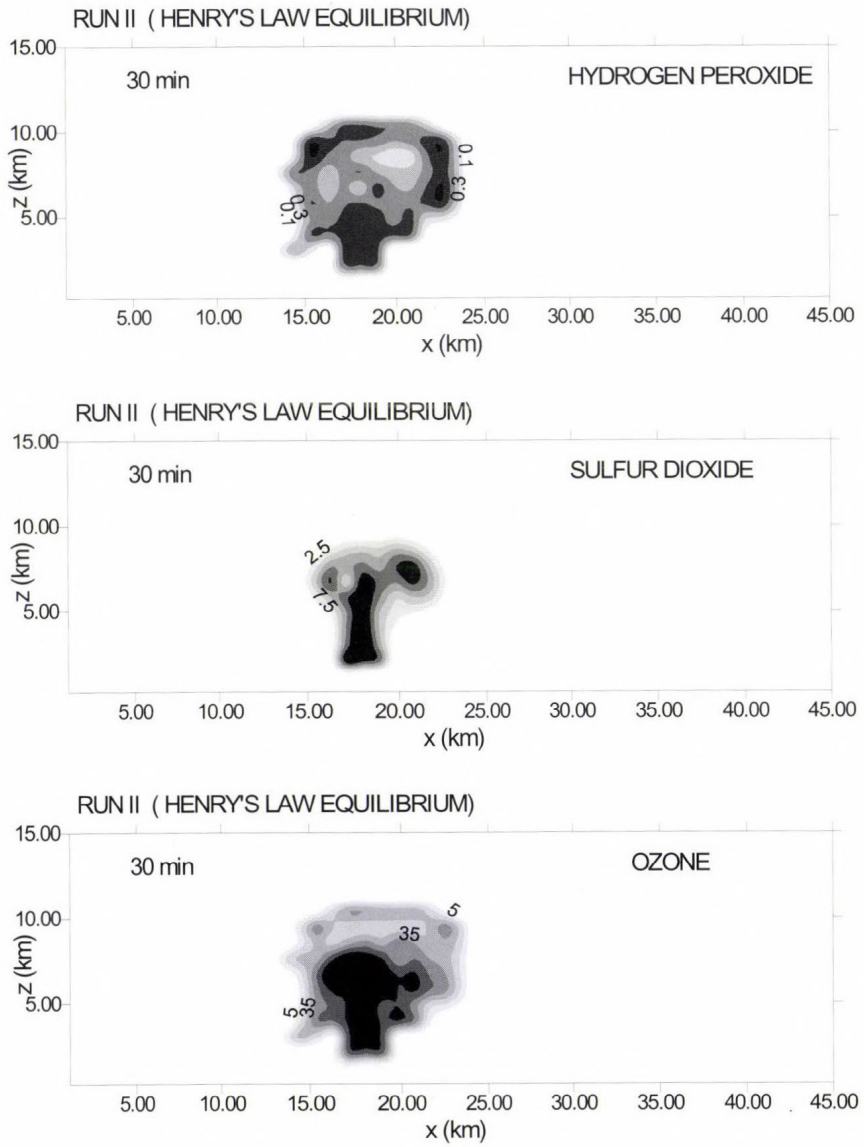

Fig. 9b. Time evolution of H_2O_2, SO_2, and O_3 concentrations in ($\mu g\ m^{-3}$) in x–z plane at $y=8$ km, in 30 min. of the simulated cloud on July 6, 1995, using Henry's Law assumption.

Examination of the SO_4^{2-} fields provides information about the integrated aerosol scavenging, i.e., nucleation scavenging, Brownian diffusion by cloud droplets, and dynamic-impact scavenging by falling hydrometeors. In-cloud

scavenging of SO_4^{2-} and NH_4^+ parallel, providing that the ratio SO_4^{2-}/NH_4^+ remains constant. Sub-cloud scavenging is also a linear function of the local aerosol concentration and non-linear function of precipitation rate. Since the NH_4^+ and SO_4^{2-} aerosol fields have identical collection efficiency (11.0), scavenging of SO_4^{2-} aerosol in the sub-cloud region will take place parallel with the NH_4^+ sub-cloud scavenging.

In-cloud scavenging for distributions in continental non-polluted and polluted cases is responsible for about 27% and 20% of the total production, respectively. Sub-cloud scavenging for those types of clouds contributes about 35% and 29%, respectively. Values in *Table 6* indicate that about 30% of the NH_4^+ in precipitation is from in-cloud scavenging, and that about 23% is from sub-cloud scavenging.

In-cloud scavenging processes in *Taylor* (1989b) accounted for 30–50%, while sub-cloud scavenging contributed for about 25%. These higher calculated percentage numbers, especially for in-cloud scavenging, are attributed to one-dimensionality of the model used, and to the assumed Henry's law equilibrium, which leads to strong scavenging of gases.

4.3 The relative importance of oxidation in sulfate production and wet deposition

Reactions, which evolve during oxidation of S (IV) to S (VI) by H_2O_2 and O_3, are of particular interest of cloud chemistry. In order to estimate the relative contribution of SO_2 oxidation, two experiments were set up. The first one was accomplished using the entire chemistry parameterization discussed in paper by *Spiridonov* and *Curic* (2003), while the second turned off all oxidation terms, i.e., PS2, PS9, PH20, OHP20, PH21, and OHP21. *Fig. 10a* shows time series of SO_4^{2-} aerosol distributions obtained by the oxidation off run, in the mature and heavy precipitation stages of the storm evolution. Plots shown in *Fig. 10b* represent distribution by oxidation off run. As it can be seen in *Fig. 10a*, inclusion of oxidation terms gives relatively higher in-cloud and sub-cloud SO_4^{2-} concentration values almost everywhere in the domain. It suggests that possible enhanced oxidation in convective clouds may act as an important source of sulfate in the air, as illustrated by the time evolution of the integrated sulfate concentration.

In-cloud oxidation of S (IV) to SO_4^{2-} is a function of aerosol composition and accounts for about 35% in the non-polluted clouds and about 32% in the polluted ones. Sub-cloud oxidation contributes to 40% and 35% of the total sulfur mass removed by wet deposition in the case of non-polluted and polluted

clouds, respectively. Oxidation of SO_2 accounts for about 15% of the in-cloud SO_4^{2-}. These results are in quite good agreement with those of *Wang* and *Prinn* (2000). Their calculations indicate that about 9.0% of dissolved SO_2 have been converted into aqueous sulfuric acid for 30 hours simulation. As a result, the aqueous processes only contribute 21% to the total sulfate production. A slightly higher estimated value of our study (15%) in light of *Wang* and *Prinn* (2000) is probably attributed to different model initializations and using low ozone (10 ppb) in the initial profile of O_3 mole fraction.

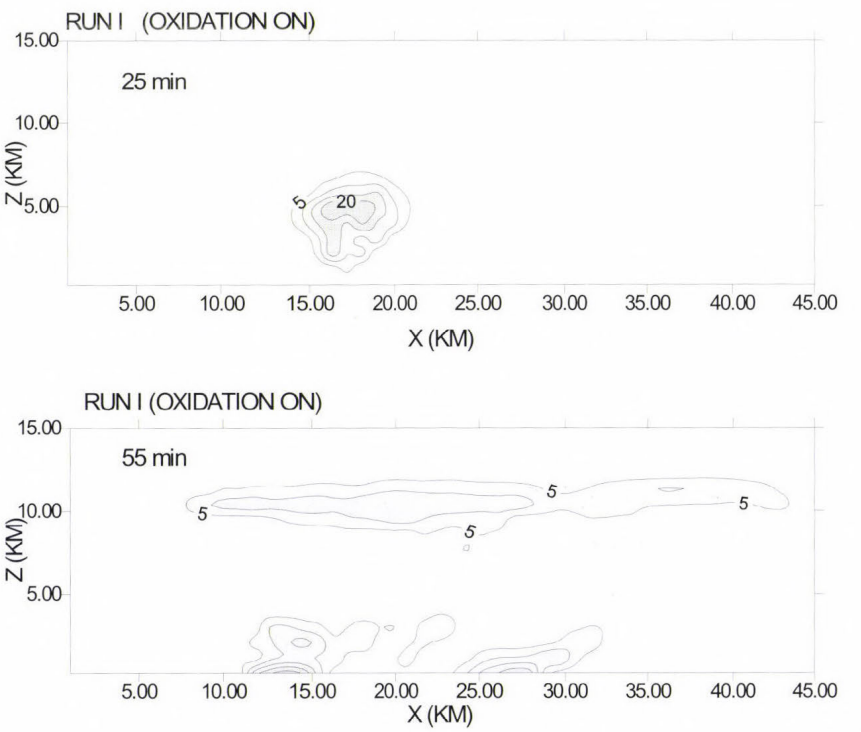

Fig. 10a. Time evolution of the sulfate concentration (μg m^{-3}) in the $x-z$ plane at $y = 8.0$ km, in 25 and 55 min. Panels represent sulfate distribution by oxidation on run.

It is also interesting to compare the results here to those in *Taylor* (1989b), where in-cloud oxidation of SO_2 contributed to 10% and 25% of the total sulfur mass deposited, while sub-cloud oxidation accounted for about

10% and 35% for continental non-polluted and continental polluted clouds, respectively. These values seem to be overestimated, as the result of implicit treatment of gases included in chemistry scheme and assumed Henry's law equilibrium. Finally, the integrated sulfur mass removed by wet deposition for continental non-polluted and continental polluted distributions of our study accounted for about 8.12 and 26.20 kg, respectively, and are similar to estimated values (7.35 and 24.35 kg) in *Taylor* (1989b).

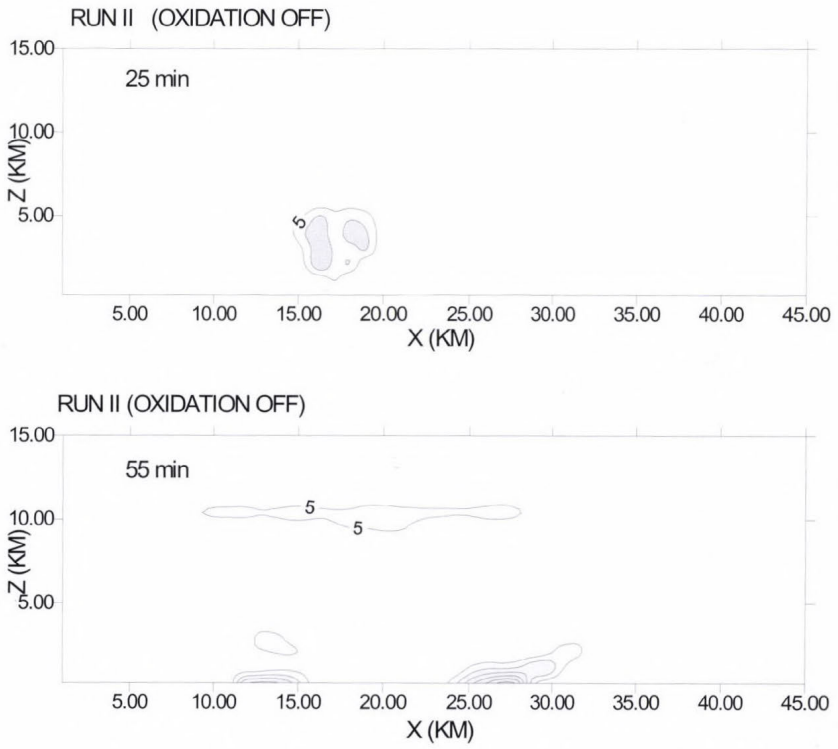

Fig. 10b. Time evolution of the sulfate concentration ($\mu g\ m^{-3}$) in the $x-z$ plane at $y = 8.0$ km, in 25 and 55 min. Panels represent sulfate distribution by oxidation off run.

4.4 The role of the ice phase processes

Table 7 lists the dominant production terms for rain, snow, and hail that control the microphysical processes for the summer case simulation of July 6, 1996. As it can be seen, most of the precipitation in the simulated convective

clouds came from the ice-phase processes. The key microphysical processes that transfer the dissolved species to the resultant frozen hydrometeor are the accretion of cloud water by snow (PSACW), accretion of cloud ice by snow (PSACI), depositional growth of snow (PSDEP), wet and dry growth of graupel (PGDRY, PGWET), accretion of cloud water by graupel (PGACW), and auto-conversion (aggregation) of snow (PGAUT). Conversion of cloud water to ice phase terminates the aqueous phase sulfate reactions. Collision of super-cooled droplets with solid ice and riming leads to the efficient retention of sulfate. In order to study the effects of ignoring the ice phase upon the chemistry, a series of test were made in which the cloud dynamics and microphysics were not changed, but the chemical reactions in the frozen hydrometeors were assumed to be identical to those in precipitation water. Neglecting liquid-ice phase leads to overestimation of the total sulfur mass removed by wet deposition of about 148% for continental non-polluted and around 133% for continental polluted distributions, relative to the base run.

Table 7. The dominant transfer rates for the microphysical processes for the summer case simulation on July 6, 1995

Rain ($g\,g^{-1}s^{-1}$)		Snow ($g\,g^{-1}s^{-1}$)		Hail ($g\,g^{-1}s^{-1}$)	
PRAUT	0.0	PSAUT	0.0	**PGAUT**	$0.6\cdot10^{-7}$
PRACW	0.0	**PSACI**	$0.2\cdot10^{-5}$	PGFR	$0.3\cdot10^{-9}$
PIACR	0.0	**PSACW**	$0.5\cdot10^{-5}$	**PGACW**	$0.3\cdot10^{-5}$
PSACR	$0.9\cdot10^{-6}$	PSACR	$0.3\cdot10^{-11}$	PSACR	$0.4\cdot10^{-11}$
PGARR	$-0.3\cdot10^{-14}$	PSFW	$0.4\cdot10^{-13}$	**PRACS**	$0.3\cdot10^{-5}$
PGFR	0.0	PSFI	$0.1\cdot10^{-12}$	PRACI	$0.2\cdot10^{-19}$
PSMLT	$-0.7\cdot10^{-10}$	PIACR	$0.6\cdot10^{-16}$	PGACR	$0.2\cdot10^{-11}$
PREVP	$-0.2\cdot10^{-5}$	**PSDEP**	$0.3\cdot10^{-6}$	PGACRP	$0.4\cdot10^{-10}$
PRAUT	0.0	PSMLT	0.0	PIACR	$0.1\cdot10^{-16}$
PRACW	0.0	PGACS	0.0	PGSUB	0.0
PSACW	0.0	PGAUT	$0.4\cdot10^{-7}$	PGACS	$0.2\cdot10^{-5}$
PGACW	0.0	**PRACS**	$0.8\cdot10^{-6}$	**PGDRY**	$0.3\cdot10^{-5}$
PGMLT	$-0.2\cdot10^{-5}$	PSSUB	$-0.2\cdot10^{-7}$	PGWET	$0.8\cdot10^{-4}$

5. Summary and conclusions

A three-dimensional interactive cloud dynamics, microphysics, and chemistry model has been used to simulate the sulfate transport and redistribution by deep convective clouds.

The summer case simulation has shown generation of strong vertical upward and downward air motions, intensive cloud evolution, microphysical transformations, and occurrence of extensive precipitation. The simulation demonstrated that the local air mass thunderstorm can significantly change the spatial distribution of sulfate aerosol concentrations. The formation of ice phase can greatly modify the relative efficiency of aqueous reactions, and thus modify the changes in chemical properties induced by deep convection. The early formation of precipitation and enhanced scavenging contributed to the build-up of approximately 2.5 times greater equivalent air concentration of sulfate in precipitation near the surface than that found in the air at this level. The key microphysical processes that transferred the dissolved matter to the resultant frozen hydrometeor were the accretion of cloud water by snow, accretion of cloud ice by snow and depositional growth of snow, wet and dry growth of graupel, accretion of cloud water by graupel, and auto-conversion (aggregation) of snow.

The spring case numerical experiment with chemical background taken from Macedonia provided insight into the potential influence on the long-range transport of atmospheric pollutants, and ascertained some semi-quantitative and semi-qualitative hypotheses about processes by which acidic species are incorporated into precipitation. The model computed sulfate concentration and wet deposition are in fairly good agreement with observations. The average equivalent cloud water pH and rainwater pH, when more acid precipitation occurs, are about 5.0 and 4.5, respectively.

The performed sensitivity tests have revealed that nucleation and aerosol in-cloud scavenging account for about 30% and 20% of the total sulfur mass removed by wet deposition, for continental non-polluted and polluted clouds, respectively. Sub-cloud scavenging contributed to 35% and 29% of the total sulfur mass deposited. Liquid-phase in-cloud oxidation contributes to about 35% and 32%. Sub-cloud oxidation in those types of clouds accounted for about 40% and 35%, respectively. Neglect of the ice phase when considering chemistry in continental non-polluted and continental polluted clouds may lead to overestimation by about 140% and 150% of the total sulfur mass removed by wet deposition. The assumption of Henry's law equilibrium for those types of clouds gives overestimation of about 148% and 133%, respectively.

Many questions related to the impact of deep convection on redistribution of atmospheric pollutants remain unanswered. Our next task is to improve the

model chemistry by including more detailed gaseous phase physics and chemistry, better initialization without random parts, parameterization of radiation, as well as surface chemical processes.

Acknowledgements—First of all we acknowledge to *Mr. Bosko Telenta* for his support, giving insights, and explanations concerning the technical aspects of his model. We also wish to express our gratitude to *Professor Dragan Markovic* of the University of Belgrade for his suggestions and advice during development of the chemistry part of the cloud model. The anonymous referees have made many substantial remarks that increased the completeness and clarity of the manuscript. We would like to express our special gratitude to *Dr. Tamás Práger* for his important contribution giving constructive comments during final revision of the paper.

References

Andreevska, M., Spiridonov, V., and *Cvetkovic, J.*, 2001: Dust transport and deposition in FYROM in April 2000. *J. Environmental Protection and Ecology 2,* 704-716.

Curic, M., Janc, D., and *Vuckovic, V.*, 1999: The effects of the hail suppression seeding simulated by the two-dimensional convective cloud model. Seventh WMO Scientific Conference on Weather Modification, Thailand, *WMO/TD-No. 936, Vol. II*, 515-518.

Durran, D.R., 1981: The effects of moisture on mountain lee waves. *Ph.D. Thesis*. Massachusetts Institute of Technology Boston, MA(NTIS PB 82126621).

Hsie, E.Y., Farley, R.D., and *Orville, H.D.*, 1980: Numerical simulation of ice-phase convective cloud seeding. *J. Appl. Meteor. 19*, 950-977.

JICA, 1999: The study on air pollution monitoring system in FYROM. Final report (draft).

Klemp, J.B. and *Durran, D.R.*, 1983: An upper boundary condition permitting internal gravity wave radiation in numerical mesoscale models. *Mon. Wea. Rev. 11*, 430-444.

Nickovic, S., Spiridonov, V., Andreevska, M., and *Music, S.*, 2000: Simulation and measurements of dust deposition in Macedonia. *Proc. 15th International Conference on Nucleation & Atmospheric Aerosols (AIP)*. Rolla, Missouri, Arizona, USA.

Spiridonov, V. and *Telenta, B.*, 2000: Numerical simulation of propagation of air pollution released from coal power plant during snowstorm. *Proc. 13th Int. Conf. on Clouds and Prec., Vol. I.* Reno, Nevada, USA, 902-905.

Spiridonov, V. and *Curic, M.*, 2003: Application of a cloud model in simulation of atmospheric sulfate transport and redistribution. Part I. Model description. *Időjárás 107,* 85-114.

Taylor, G.R., 1989b: Sulfate production and deposition in midlatitude continental cumulus clouds II, Chemistry model formulation and sensitivity analysis. *J. Atmos. Sci. 46,* 1991-2007.

Telenta, B. and *Aleksic, N.*, 1988: A three-dimensional simulation of the 17 June 1978 HIPLEX case with observed ice multiplication. *2nd Int. Cloud Modeling Workshop. WMO/TD,* No. 268, Toulouse, 277-285.

Tremblay, A. and *Leighton, H.*, 1986: A three-dimensional cloud chemistry model. *J. Climate Appl. Meteor. 25*, 652-671.

Wang, C. and *Prinn, R.G.*, 2000: On the roles of deep convective clouds in tropospheric chemistry. *J. Geophys. Res. 105,* 22,269-22,297.

IDŐJÁRÁS

Quarterly Journal of the Hungarian Meteorological Service
Vol. 108, No. 2, April–June 2004, pp. 123–140

An estimate of the influence of climate change on heating energy demand in regions of Hungary, Romania, and Finland

Andrea Vajda, Ari Venäläinen, Heikki Tuomenvirta and **Kirsti Jylhä**

Finnish Meteorological Institute, Meteorological Research,
P.O. Box 503, FIN-00101 Helsinki, Finland; E-mail: claudia.vajda@fmi.fi

(Manuscript received February 27, 2002; in final form July 1, 2003)

Abstract—In this study the impacts of predicted anthropogenic climate change on heating energy demand in some regions of three European countries are estimated. The countries studied are Hungary, Romania, and Finland. The estimate is obtained by examining the projected future values of the heating degree-days (HDD) index, a measure widely used for assessing heating energy consumption. Estimates of climate change are obtained from two coupled atmosphere-ocean general circulation model runs, conducted by the HadCM3 and the ECHAM4/OPYC3 models. The results suggest a 10–14% decrease in heating energy demand during the next 50 years in the three studied countries. Though there are still uncertainties related to the magnitude of climate warming, the negative trend in heating energy demand seems so evident, that it should be taken into account in the planning of future energy management.

Key-words: climate change, heating degree-days index, heating energy demand, energy and climate.

1. Introduction

The anticipated air temperature rise due to anthropogenic climate change will have several impacts on the energy sector (e.g., *Darmstadter*, 1993). Higher temperatures lead to reduced heating energy demand during the winter seasons, and in some regions to an increased cooling energy demand during summers, although, the estimate of the net effect is scenario- and location dependent. Some energy production and distribution systems may experience adverse impacts that would reduce supplies or system reliability, while other

energy systems may benefit. The availability of hydro-, wind-, and solar power may change if precipitation, evaporation, wind and cloudiness undergo changes. Changes in river flow regimes, greater probability of drought and less precipitation falling as snow may reduce the hydroelectric capacity of current powerhouses. Increased cloudiness can reduce solar energy production. Wind energy production would also be reduced if wind speeds increased above or fall below the acceptable operating range of available technology (*IPCC*, 2001a,b). Global warming may also affect the energy sector. For example, the efficiency of condensing power plants may decrease, the rise of the cooling water temperature (taken from oceans and continental waters: rivers, lakes) may produce this negative influence additionally. The amount of available bioenergy may increase as the speed of forest growth increases (e.g., *Kellomäki*, 1993).

The HDD index is the sum of the differences between daily mean outdoor temperature and indoor temperature. It has been found to be a good measure for estimating heating energy consumption (e.g., *Quayle* and *Diaz*, 1980). The HDD index has been used as an estimate for heating energy demand in several research projects. For example, *Cvitan* and *Poje* (1985) estimated the degree of coldness in Croatian winters using the number of heating days and the heating degree-days. *Hargy* (1997) constructed objective mapping of the spatial variation of degree-days for Ireland applying statistical models of spatial variation to a digital terrain model of Ireland. These maps were then used to identify areas with anomalous temperature regimes. *Kadioglu et al.* (1999) studied heating degree-days in Turkey and represented maps of spatial degree-days distribution; these were then related to various climatic, meteorological, and topographic features of Turkey. Studies on heating degree-days were conducted in Czech Republic by *Starostova* (1999). The study examined the heating period characteristics in south Bohemia for the period 1961–1997, when the annual sums of degree-days showed a slight regressive trend.

In North America, *Soule* and *Suckling* (1995) examined the temporal trends and spatial variability of heating and cooling degree-days in a region of south-eastern USA for the period 1960–1989 using time series analysis, regression analysis, and a climate departure index. Their results showed a weak downward trend for actual heating degree-days values across the region during the studied period. *Darmstadter* (1993) studied climate change impacts on the energy sector and energy supply in the MINK region (Missouri, Iowa, Nebraska, and Kansas states). He illustrated that a 0.65–0.90°C rise in temperature results in a 5–8% decline in heating degree-days and a 20–40% rise in cooling degree-days. In Canada, the HDD values during the period 1990–1998 showed a significant negative trend. Heating degree-days, as simulated by the first version of Canadian Global Coupled Model (CGCM1) in

the GHGA runs, may decrease by 25–50% over northern landmasses by the year 2100 (*Kharin* and *Zwiers*, 2000).

The scope of the present research is to estimate the possible future change in the heating energy demand for two regions, Finland in northern Europe and parts of Hungary (Great Hungarian Plain) and Romania (Transylvanian Basin) in Central and East Europe. Within the studied regions, *Tistea* (1974) has determined the monthly HDD values for Romania and identified the regions. In Hungary, *Ambrózy* and *Faragó* (1988) analyzed the effect of severe meteorological conditions, especially the unusually cold winter periods, on the energy supply and demand. They introduced some additional tasks which pertain to energy problems that might arise under severe meteorological conditions. *Faragó et al.* (1991) studied the global and regional changes of climate and impacts of these, as well as the climatic sensitivity of the energy demand and consumption. According to their results, the climatic change will have essential impact upon the energy demand and consumption: 1°C change in the mean winter temperature would cause a change of 6% of opposite sign in the domestic energy use for heating purposes.

In Finland, *Kuivalainen et al.* (1996) conducted a study of the impact of climate change on the energy production and consumption. Their results suggest a significant decrease in the need for heating energy (25% by 2100) and an increase in the energy-supply (5% for hydroenergy capacity by 2100). Their study was based on two climate scenarios: the Finnish Research Programme on Climate Change, SILMU (*Carter et al.*, 1995), and the Nordic project (*Jonsson et al.*, 1994). *Sælthun et al.* (1998) have also studied the climate change impacts on the energy consumption and hydropower production in Nordic countries. For Finland they determined a 2.4% reduction in the electricity demand by 2050. In the current study the estimates for the magnitude of climate warming are obtained from two transient climate change simulations, performed with coupled atmosphere-ocean general circulation models: HadCM3 (e.g., *Gordon et al.* (2000) and *Pope et al.* (2000)) and ECHAM4/OPYC3 (*Roeckner et al.*, 1999). The period studied is the first half of the 21st century (2000–2050). Measured data (1901–1999) were used to obtain an indication in the natural variation of the HDD index.

Population-weighted heating degree-days are often used, as they reflect the combined effects of climate fluctuations and population movements (*Downton et al.*, 1988; *Taylor*, 1981). Besides population, the heating energy consumption also depends on building construction. For example, new buildings may have better insolation, and thus energy consumption is less than in older buildings. The volume of building stock also affects the absolute heating energy demand; the increase in building stock during the study period causes more heating energy demand. However, this paper does not study how

the population will develop, how the volume of building stock will change, or how construction techniques will develop in the future. These issues are beyond the scope of the paper, we will concentrate on climate related aspects that also contain a number of uncertainties.

2. Data and methods

2.1 The calculation of heating degree-days

The heating degree-days index (HDD) is the sum of the differences between daily mean outside temperature (Tdaily) and inside temperature. There are different ways to calculate HDD index, for example, sometimes daily maximum and minimum outside air temperatures are used instead of daily mean temperature. The inside or base temperature is adopted according to historical convention, quite often 15°C is used (*Heerdegen*, 1988). In Scandinavian countries the inside temperature is estimated to be 17°C, and thus monthly HDD index can be calculated using Eq. (1),

$$HDD = \sum_{i=1}^{n} [-(Tdaily_i - 17)], \tag{1}$$

where n is the number of days per month. In the January–June period HDD values will not be zero if *Tdaily* is less than 10°C, while in July–December if *Tdaily* is less than 12°C. These limits are defined based on the assumption that during the first half of the year, the heating of buildings due to solar radiation is greater, as there are usually fewer clouds than in the second half of the year. The method explained here is found to give a good interpretation of the heating energy demand and used routinely by energy producers in Scandinavian countries.

The HDD index is conventionally calculated on the based of daily values. As only monthly data were available from Global Spectral Model (GSM) runs, we first studied if it would be possible to calculate HDD using only monthly mean temperatures. HDD values, calculated with monthly and daily data, are strongly correlated — for example, the correlation coefficient at two Finnish stations, Helsinki and Sodankylä (*Fig. 1*) was 0.993 and 0.995, at the Romanian station, Târgu-Mures it was 0.989 (*Fig. 1*). Due to the strong correlation, it was justified to use monthly mean temperatures for the calculation of the HDD index,

$$HDD = -(Tmonthly - 17)\, n, \tag{2}$$

where n is the number of days per month. Seasonal and annual HDD index values were calculated using monthly HDD index values. During the winter season, when temperatures are below cut-off limits, 10 and 12°C, the difference between values calculated using daily and monthly data is negligible, but during other seasons, the HDD index values obtained from monthly data may be somewhat smaller than if daily data were used (see *Table 1*). An apparent reason is that the period between spring and autumn includes months, when temperatures are over the cut-off limits (10–12°C). However, as most of the heating energy demand appears during the winter season, when the temperature is clearly below the cut-off limits, the difference between values calculated from monthly and daily data is insignificant.

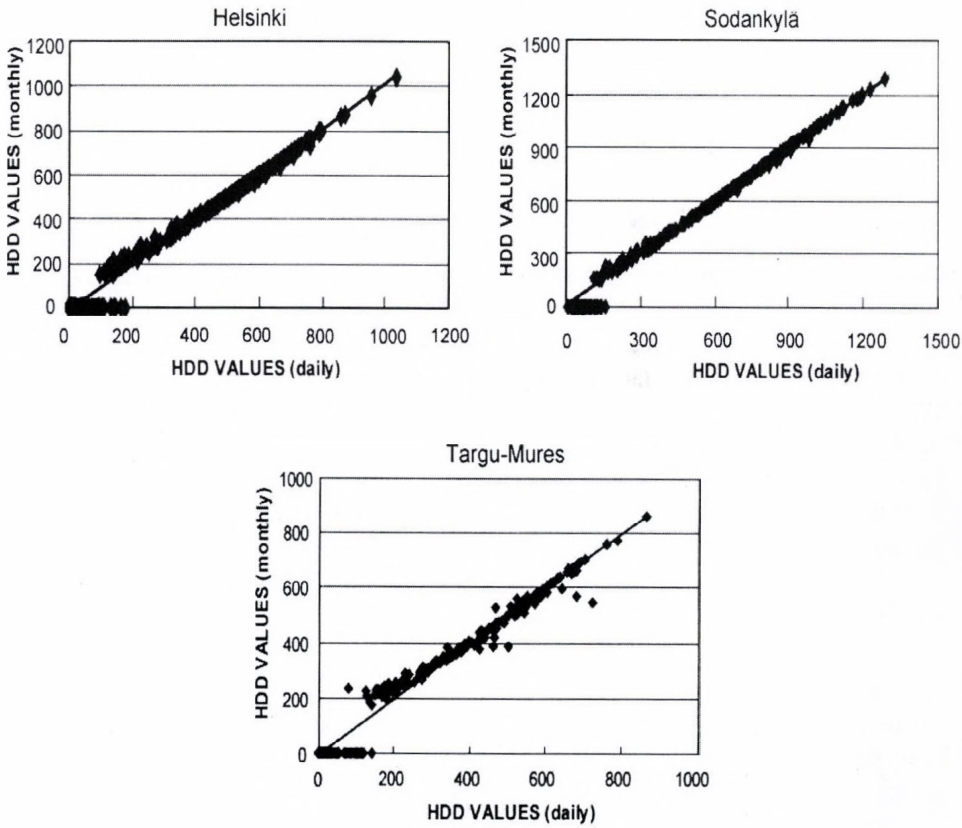

Fig. 1. Monthly HDD index calculated using daily (x-axis) and monthly (y-axis) mean temperatures in Helsinki, Sodankylä, and Târgu-Mures in 1970-1999.

Table 1. The mean seasonal and annual HDD index values calculated using all available (Fig. 3) monthly mean temperatures

Stations	Annual	Oct–Mar	Apr–Sep	Winter	Spring	Summer	Autumn
Jyväskylä	4727	3836	891	2213	1308	11	1195
Helsinki	4102	3347	755	1928	1211	0	962
Kuopio	4961	3994	967	2308	1390	11	1252
Vaasa	4623	3643	980	2069	1388	16	1150
Sodankylä	6256	4750	1506	2684	1753	213	1605
Békéscsaba	2498	2428	70	1563	430	0	505
Debrecen	2622	2534	88	1600	456	1	564
Túrkeve	2550	2481	69	1586	430	0	534
Cluj-Napoca	3028	2821	207	1756	606	0	666
Bistrita	3079	2855	224	1761	623	0	695
Dej	3021	2839	182	1762	593	0	666
Târgu-Mures	2931	2775	156	1740	546	2	642
Turda	3005	2811	194	1748	588	0	668

2.2 Estimation of heating degree-days applying general circulation models

Estimates of the magnitude of projected climate warming were obtained from two general circulation models: HadCM3 developed at the Hadley Centre (UK; see *Gordon et al.*, 2000; *Pope et al.*, 2000) and ECHAM4/OPYC3 developed at the Max-Planck-Institute for Meteorology and German Climate Computing Centre (DKRZ, Germany; see *Roeckner et al.*, 1999). In this present study we used an all-anthropogenic forcing integration (AA) by HadCM3 and a sulfate aerosol and greenhouse gas experiment (GSD) by ECHAM4/OPYC3. In addition to warming due to enhanced concentrations of greenhouse gases, both these simulations include an estimate of the cooling influence of anthropogenic sulphate aerosols due to backscattering of solar radiation in clear skies (direct effect). The HadCM3-AA simulation also estimates the impact of sulfate aerosols on cloud albedo (indirect effect), as well as radiative forcing due to anthropogenic changes in the tropospheric ozone. From 1860 to 1990, radiative forcing is calculated on the basis of observations. From 1990 onward, HadCM3-AA uses the IS95a emissions scenario, and ECHAM 4/OPYC3-GSD applies the IS92a emissions scenario.

A 90-year simulation starting from the year 1961 was used for both models. The 90-year period was divided into three 30-year periods. By comparing these 30-year periods, it was possible to obtain an estimate how the HDD index may change in the near future. The grid sizes of the global models

HadCM3 and ECHAM4/OPYC3 are 2.5×3.75° and 2.8×2.8° (latitude-longitude), respectively. These correspond roughly to 200–300 km at the latitudes studied (*Fig. 2*). For this study we selected 9 (4 from HadCM3 and 5 from ECHAM4) grid squares for Finland and 6 (3 from HadCM3 and 3 from ECHAM4) grid squares for Romania and Hungary, and examined how the HDD index would change in these grid squares.

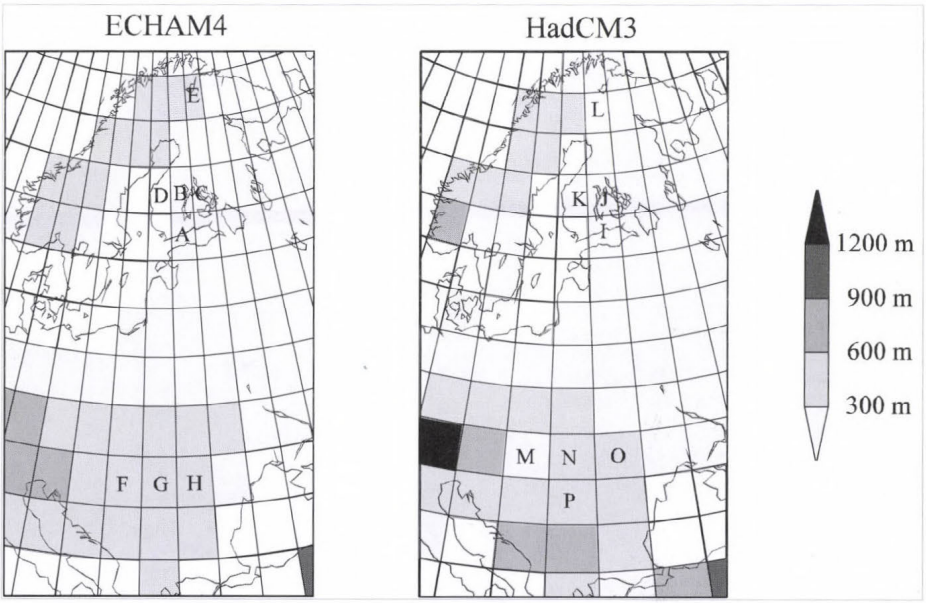

Fig. 2. The land-sea mask in the ECHAM4 and HadCM3 AOG models. The grid-squares used in the current study are named using letters A-H (ECHAM4) and I-P (HadCM3).

Grid values represent mean values over the whole grid box. To obtain an indication of how the HDD index varies naturally at certain locations, measured temperature values were studied first. Measured data covered the period 1901–1999 from 5 locations in Finland (Helsinki, Jyvaskylä, Vaasa, Kuopio, and Sodankylä), 3 locations in Hungary (Debrecen, Békéscsaba, Túrkeve), and 5 locations in Romania (Cluj-Napoca, Dej, Turda, Târgu-Mures, Bistrita) (*Fig. 3*). These weather stations belong to national meteorological networks and measurement data has been passed through quality control. The whole of Finland is represented by the stations used, while the data sources from the two other countries are located in western Romania (Transylvanian Basin) and eastern Hungary (Hungarian Plain on the left bank of Danube).

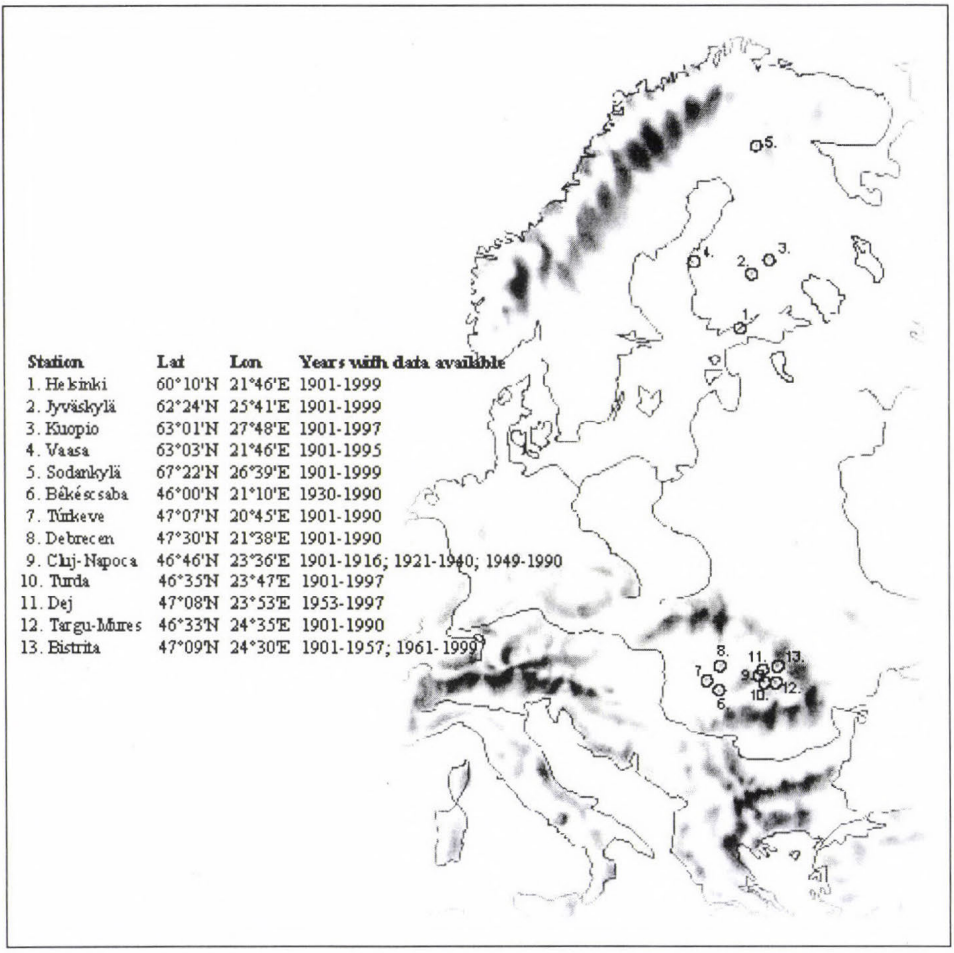

Fig. 3. Stations used in the study.

It is questionable how accurate an estimate of HDD can be, obtained using global model rather than more detailed data. If we were to examine how much the HDD index varies at certain locations, then use of global model grid square values is not a good alternative. However, in our study we are interested in how much the energy demand will change in a larger area, and in that sense the use of global model is justified, though the details of spatial variation are less well described by global models. A larger source of uncertainty than the grid size is related to the general accuracy of climate models as well as the uncertainty related to future emission scenarios.

In order to obtain an estimate of the uncertainty related to different scenarios and atmosphere-ocean general circulation model (AOGCMs) calculations, the mean wintertime (December–February) temperature changes, from 1961–1990 until 2021–2050, under the four preliminary SRES98 marker scenarios from the IPCC Special Report on Emissions Scenarios (*IPCC,* 2000; *Hulme* and *Carter*, 2000) and nine different AOGCMs model runs were determined. Based on these temperature values, the HDD index for Finland for the studied period 2021–2050 was calculated. The scenarios used give quantitative interpretations for four alternative storylines (A1, A2, B1, B2) representing possible futures with different driving force combinations. Further, a scaling method (*Hulme* and *Carter*, 2000) was used to estimate the range of regional climate projections arising from the uncertainties in emissions and climate system response. B1-low assumes low emissions and low climate sensitivity; A1-mid and B2-mid are based on central estimates; A2-high assumes high emissions and high climate sensitivity. The adopted AOGCMs were CGCM1 (*Flato et al.*, 2000), CSIRO-Mk2 (*Gordon* and *O'Farrell*, 1997), HadCM2 (four ensemble runs) (*Johns et al.*, 1997), HadCM3 (*Gordon et al.*, 2000; *Pope et al.*, 2000), NCAR DOE-PCM (*Washington et al.*, 2000), ECHAM4 (*Roeckner et al.*, 1999). The mean temperature of Finland (*TF*) was defined as the mean of temperatures in the grid squares (*Tsq)* covering the country.

$$TF = \frac{\sum_{i=1}^{nu} Tsq_i}{nu}, \tag{3}$$

where *nu* is the number of grid squares covering Finland. The mean HDD index for the Finnish locations in 2021–2050 ($HDD_{2021-2050}$) was calculated by rising the mean 1901–1999 temperature as indicated by different models and scenarios.

$$HDD_{2021-2050} = [17 - (TW_{1901-1999} + \Delta T)]\,90, \tag{4}$$

where $TW_{1901-1999}$ is the mean temperature for period 1901–1999, calculated as the mean of the five stations (Helsinki, Jyväskylä, Kuopio, Vaasa, and Sodankylä) used in this study, ΔT is the temperature rise predicted by the different scenarios and models, and 90 indicates the number of days during the three-month period (December–February). This estimate is cruder than that based on monthly data, but it still provides an estimate of the limits of uncertainty involved.

3. Results

3.1 The variation of monthly and seasonal heating degree-days index values

Let us first look at the HDD index values in present day climate. Due to the cooler climate, the HDD values calculated using the measurements of the past 100 years are higher in Finland. The annual value is 1000–2000°C higher than in the other study areas (*Table 1*, see also Fig. 6). The values at stations in Hungary and Romania are close to each other. In the Romanian locations they are about 10% higher, partly due to the geographic position and orography: the mean elevation is about 300–400 m higher in the Transylvanian Basin than in the Hungarian Plain.

When examining the season-based HDD values at the studied stations, it was found that in the winter half of the year (October–March) the highest value is 4750°C at Sodankylä, while the lowest in Finland, at Helsinki, is 3347°C. In Jyväskylä, Vaasa, and Kuopio, the values are within the 3640–3995°C range. In Hungary, the long term mean values for the winter half of the year are within the 2420–2540°C range, and in Romania the values are somewhat higher within the 2770–2850°C range (*Table 1*).

For the summer half of the year (April–September), the values are very low in Hungary (70–88°C), the dominant value is zero for the April–September period (some exceptions are recorded for April). In Romania, the HDD values follow the same pattern, but the zero-period is shorter (May–August). In Finland, extreme values are recorded again in Sodankylä (1506°C, the highest) and in Helsinki (755°C, the lowest) with values in the 890–980°C range at the other stations.

To depict how the HDD index values based on measurements are related to values obtained from climate scenarios, we divided the monthly HDD values obtained from the HadCM3 scenario (1961–2050 period) into three thirty-year periods (1961–1990, 1991–2020, and 2021–2050) and plotted them to the same figure with the values based on measurements. For the analyses we selected one station from each country: Jyväskylä from Finland, Debrecen from Hungary, and Cluj-Napoca from Romania (*Fig. 4*).

In the case of the Great Hungarian Plain and Transylvanian Basin, the HDD values based on the HadCM3 simulation for 1961–1990 period are relatively close to measurements. For Finland, the HadCM3 model predicts systematically lower temperatures than those indicated by the measurements. Due to the natural climate variation in the 1991–2020 or even 2021–2050 scenario periods, during a few months higher HDD index values are shown than in the 1961–1990 period, e.g., in January in Jyväskylä.

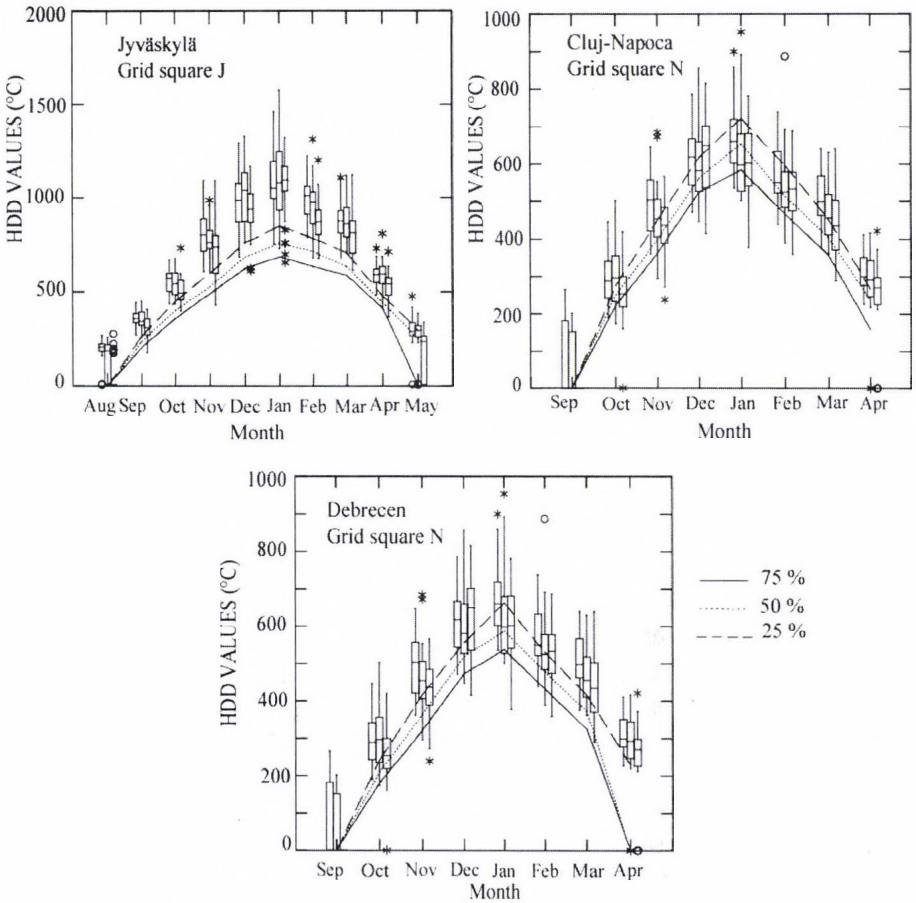

Fig. 4. Monthly HDD index values at Jyväskylä, Debrecen, and Cluj-Napoca. The line plots are 25%, 50%, and 75% percentiles based on 1901–1999 observations. The box-plots depict the variation based on the three thirty-year periods (1961–1990, 1991–2020, and 2021–2050) obtained from HadCM3 model for grid squares J and N. The horizontal line within the box corresponds to the median, the end of the box shows the interquartile range, the "whiskers" give extreme values within -1.5 and 1.5 times the interquartile range. Values outside these extreme ranges are indicated with an asterisk.

3.2 The variation in the annual heating degree-days index values

When we examine the 30-year periods of the annual HDD index (*Fig. 5*) we can see that in case of the ECHAM4 model the values are smaller than in the case of HadCM3. The latter model systematically indicates a colder climate. In Finland, the HDD indexes calculated on the base of the HadCM3 model are

approximately the same during the two periods 1961–1990 and 1991–2020, while the period 2021–2050 is clearly warmer than the two earlier periods. In the case of the ECHAM4 model, the warming of climate is slightly larger between the first and second thirty-year periods than during the second and third thirty-year periods. At all the Finnish locations, the studied HDD index values decrease on an average by 400–500°C when the 2021–2050 period is compared to the first thirty-year period 1961–1990.

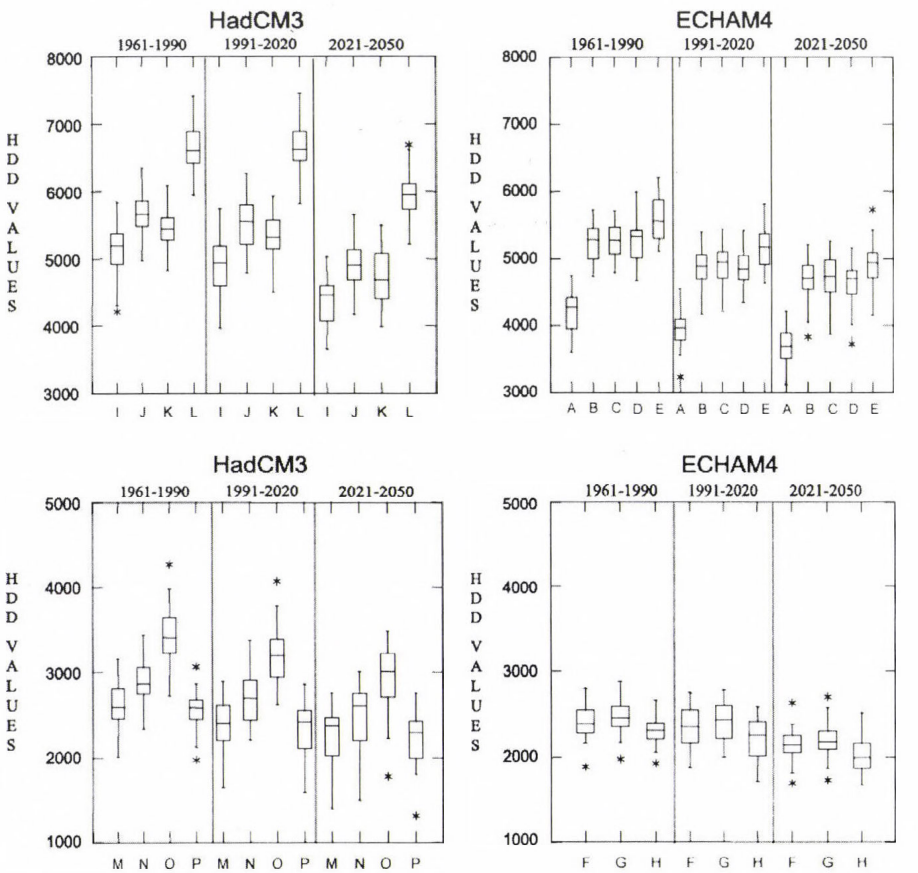

Fig. 5. The variation in annual HDD index values at grid square locations (Fig. 1) used in the study. The box-plots depict the variation based on the three thirty-year periods obtained from the HadCM3 and ECHAM4 models.

At the Romanian and Hungarian stations, the warming trend predicted by both of the models is linear. The decrease in the HDD index is about 300°C

when the 1961–1991 period is compared to the 2021–2050 period. The values in Romania are about 500–600°C higher than in Hungary, although, the stations are situated on the same latitude where the continental effect is detectable.

For the analyses of annual HDD index value changes, we have selected one reliable station from each country with long and complete data series: Jyväskylä from Finland, Túrkeve from Hungary, and Turda from Romania. Whilst examining the annual HDD index value changes during the past 100 years (*Fig. 6A*), there is a slight negative trend according to measurements (179°C in Jyväskylä). Correspondingly, the standard deviations according to measurements are 411°C (Jyväskylä), 271 (Túrkeve), and 264 (Turda).

When modeled data is examined, the negative trend in the corresponding grid squares according to ECHAM4 for the period 1950–2050 (*Fig. 6B*) is 1040, 494, 496°C in grid square B (Jyväskylä), grid square F (Túrkeve), and grid square G (Turda), respectively, and the corresponding standard deviations (trend removed from the data) are 293, 189, and 194. The natural variation of climate at the station is thus larger than the variation simulated by ECHAM4. When we examine the HadCM3 data (*Fig. 6C*), we find that in grid square J (Jyväskylä) there is no trend until 2000 and after that there is also a negative trend. The negative trend for the whole period is 1133, 593, 501°C in grid square J (Jyväskylä), grid square M (Túrkeve), and grid square P (Turda), respectively, and the corresponding standard deviations (trend removed from the data) are 390, 316, and 278. In Jyväskylä, the natural variation of climate is approximately the same in magnitude as the variation simulated by the HadCM3 model, while at other locations it is somewhat larger than the values indicated by the measurements.

3.3 The change in the heating energy demand

The change in the HDD index can be interpreted directly as a change in the heating energy demand per capita (e.g., *Quayle* and *Diaz*, 1980). According to ECHAM4, the heating energy need for the Finnish locations will decrease by 6–8% percent until the 1991–2020 period and by 10–13% until the 2021–2050 period. Using the HadCM3 values, the decrease until 2020 is only 1–4% and under 1% in northern Finland. For the latter period (after 2020), the decrease is about 10% in northern Finland and about 14% in the rest of the country (*Fig. 7*).

In the Romanian and Hungarian locations, the ECHAM4 scenario predicts a 2–4% decrease until 1991–2020 and 11–13% until 2021–2050. The HadCM3 model predicts 6–8% for the first period and 10–14% for the second period (*Fig. 7*).

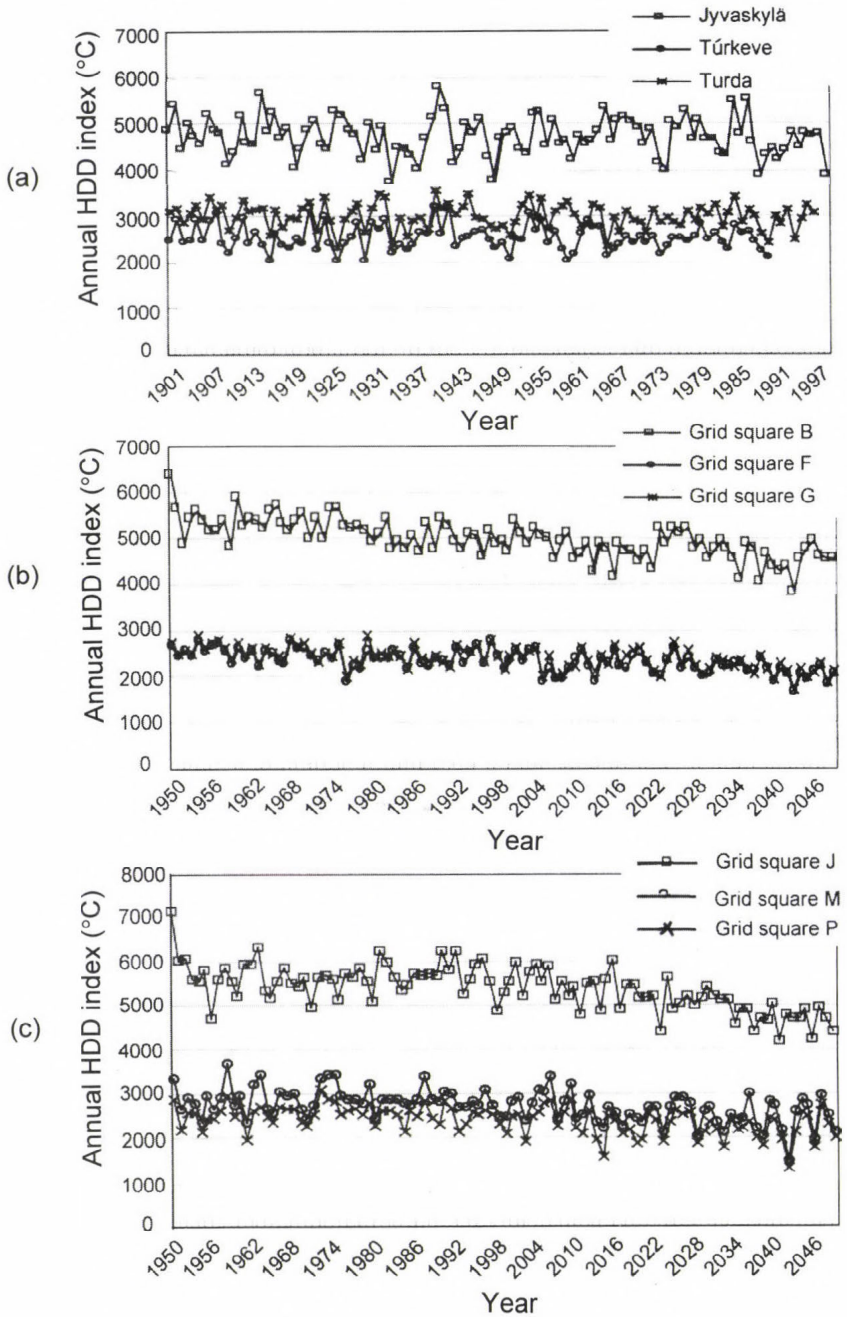

Fig. 6. Annual HDD index values calculated for three stations using: (*a*) measured monthly temperature values 1901–1999, (*b*) ECHAM4, and (*c*) HadCM3 simulations.

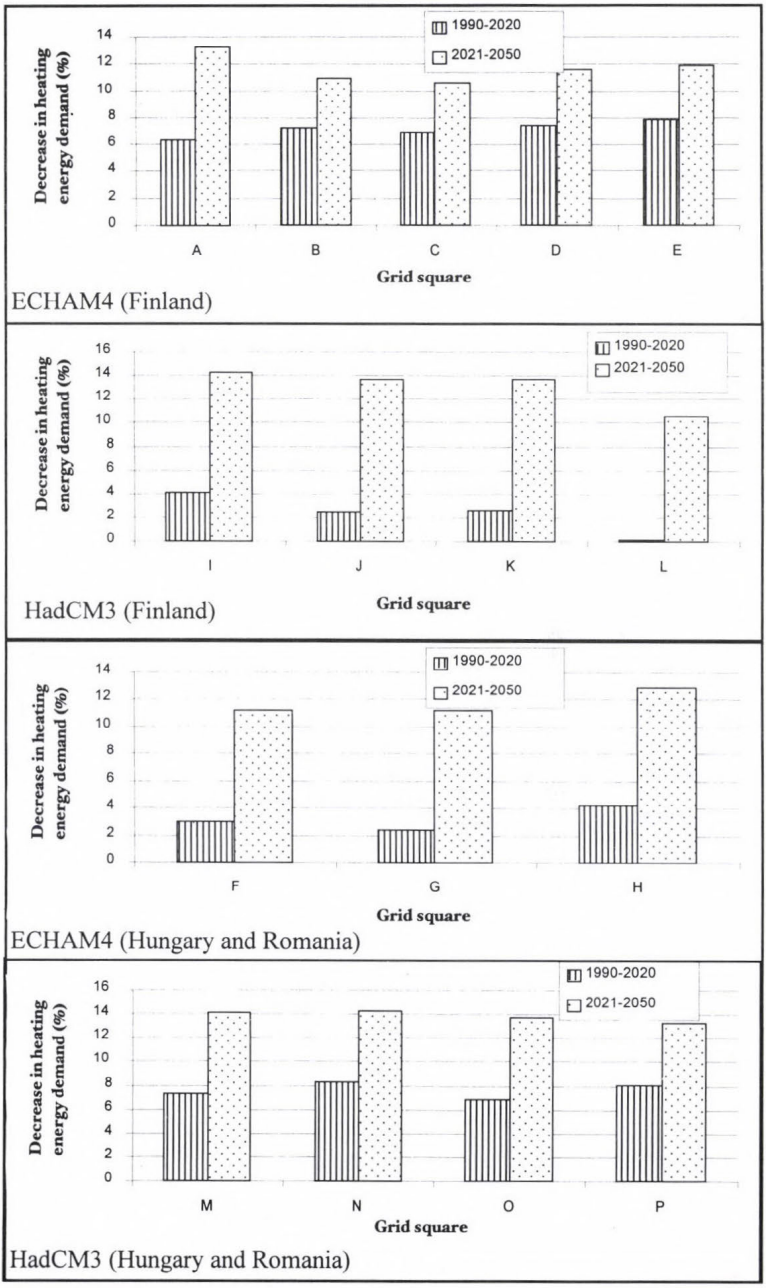

Fig. 7. The mean decrease in the heating energy demand (%) compared to the period 1961–1990, based on HadCM3 and ECHAM4 model simulations.

3.4 Estimated uncertainty

Based on the mean temperature change by 2021–2050 under the four SRES scenarios and nine different AOGCMs model runs, we determined the change in the wintertime (December–February) temperature and heating degree-days index for Finland for the studied period 2021–2050 (*Fig. 8*).

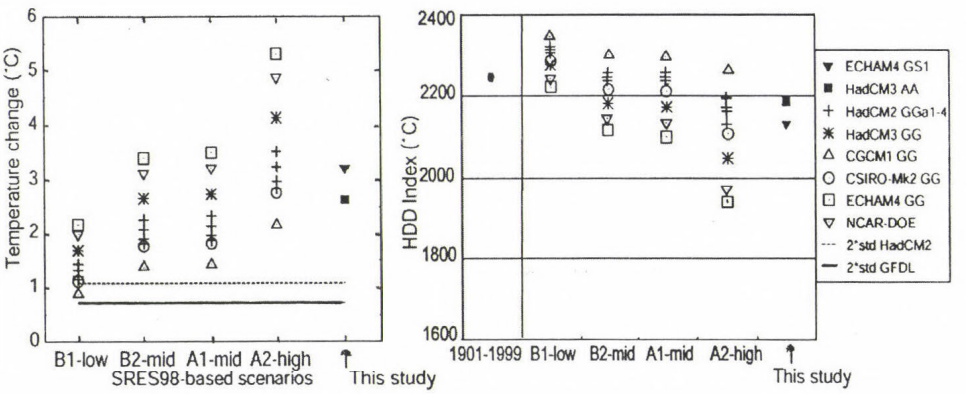

Fig. 8. The estimated climate warming from 1961–90 to 2021–2050 (*a*), and the HDD index (*b*) in Finland as obtained from nine different AOGC model simulations according to four SRES scenarios (*IPCC*, 2000; *Hulme* and *Carter*, 2000) for mid-winter months (December-February). The 2*std lines give the 2 times standard deviation values as obtained from the HadCM2 and GFDL multi-decadal simulations and depict natural climate variation. The HDD index was calculated by rising the mean 1901–1999 temperature as indicated by different simulations and scenarios (Eq. (4)). In (b) there are also HDD index values calculated on the base of the 1901–1999 mean winter temperatures included as well as the HadCM3 and ECHAM4 simulations used in the present study.

The model with the largest warming in this study was ECHAM4 and the coldest was GCCM1. The A1 and B2 scenarios showed roughly similar changes, while the decrease in the HDD index was between 100 and 300°C. The A2 scenario predicts the greatest warming with a decrease in the HDD index of between 200 and 450°C. The coldest climate would be obtained if B1-low conditions were to become true. In this case the decrease in HDD index is between 100 and 200°C.

The difference between the predicted greatest and smallest warming is still large, indicating the uncertainties related to local climate prediction and assessment studies. The HDD index change according to the results of this study corresponds to the A1-mid scenario changes, and the results are quite close to a type of predicted "average" of different models and scenarios.

4. Conclusions

The results of this study suggest that climate change will decrease the heating energy demand by 10–14% during the next 50 years. For the wintertime – when the heating energy demand is the highest – the scenarios predict a 10–12% decrease for Finland and 6–8% for the studied regions of Hungary and Romania. Though there are still uncertainties related to the magnitude of climate warming, the negative trend in heating energy demand seems so evident that it should be taken into account in the energy production scenarios.

An interesting subject to study in the future will be the probability of cold, relatively short 1-2-week periods, as the energy production capacity must be made to cover also these maximum consumption periods. Besides the heating energy demand, the climate change will inevitably also influence the cooling energy demand during summertime.

Acknowledgements—The authors wish to express sincere thanks to the reviewers of this article for their valuable comments.

References

Ambrózy, P. and *Faragó, T.*, 1988: Recent severe winters in Hungary: meteorological approach and some energy supply/demand aspects. In *Identifying and Coping with Extreme Meteorological Events* (eds: *E. Antal* and *M.H. Glantz*). Hungarian Meteorological Service, Budapest, 281-335.

Carter, T., Posch, M., and *Tuomenvirta, H.*, 1995: *SILMUSCEN and CLIGEN, Users guide*. The Finnish Research Programme on Climate Change SILMU. Publications of the Academy of Finland 5/1995.

Cvitan, L. and *Poje, D.*, 1985: Winter coldness on Croatia with regard to the number of heating days and the degree-days. *Hidrometeoroloski Zavod 20*, Rasprave, Zagreb, Yugoslavia, 65-71.

Darmstadter, J., 1993: Climate change impacts on the energy sector and possible adjustments in the MINK region. *Climatic Change 24(1-2)*, 117-129.

Downton, M.W., Stewart, T.R., and *Miller, K.A.*, 1988: Estimating historical heating and cooling needs: per capita degree-days. *J. Applied Meteorology 27(1)*, 84-90.

Faragó, T., Iványi, Zs., and *Szalai, S.* (eds.) 1991: *Climate Variability and Change, II*. Changes in composition of atmosphere and in the climatic characteristics, detection, modelling, scenarios and impacts of the regional changes (in Hungarian). Hungarian Ministry for Environment and Regional Policy — Hungarian Meteorological Service, Budapest.

Flato, G.M., Boer, G.J., Lee, W.G., Mcfarlane, N.A., Ramsden, D., Reader, M.C., and *Weaver, A.J.*, 2000: The Canadian Centre for Climate Modelling and Analysis global coupled model and its climate. *Climate Dynamics 16*, 451-467.

Gilbert, R.O., 1989: *Statistical Methods for Environmental Pollution Monitoring*. Van Nostrand Reinhold Company, New York.

Gordon, C., Cooper, C., Senior, C.A., Banks, H., Gregory, J.M., Johns, T.C., Mitchell, J.F.B., and *Wood, R.A.*, 2000: The simulation of SST, sea ice extents and ocean heat transports in a version of the Hadley Centre coupled model without flux adjustments. *Climate Dynamics 16*, 147-168.

Gordon, H.B. and *O'Farrell, S.P.*, 1997: Transient climate change in the CSIRO coupled model with dynamic sea ice. *Monthly Weather Review 125*, 875-907.

Hargy, V.T., 1997: Objectively mapping accumulated temperature for Ireland. *Int. J. Climatology 17*, 909-927.

Heerdegen, R.G., 1988: Evaluation of the heating degree-days index. *Weather and Climate 8(2)*, 69-75.

Hulme, M. and Carter, T.R., 2000: The Changing Climate of Europe. In *Assessment of Potential Effects and Adaptations for Climate Change in Europe* (ed.: *M. Parry*). Jackson Environment Institute, University of East Anglia, Norwich, UK, 47-84.

IPCC, 2000: *Special Report on Emissions Scenarios. Nakicenovic, N., Alcamo, J., Davis, G., De Vries, B., Fenhann, J., Gaffin, S., Gregory, K., Grübler, A., Jung, T.Y., Kram, T., LaRovere, E.L., Michaelis, L.*. http://www.grida.no/climate/ipcc/emission/index.htm.

IPCC, 2001a: *Climate Change-2001: The Scientific Bases*. Contribution of Working Group I. *Albritton, D.L., Allen, M.R., Baede, A.P.M., Church, J.A., Cubash, U., Xiaosu, D., Yihui, D., Ehhalt, D.H., Folland, C.K., Giorgi, F., Gregory, J.M., Griggs, D.J., Haywood, J.M.* http://ipcc-ddc.cru.uea.ac.uk/index.html

IPCC, 2001b: *Climate Change 2001: Impacts, Adaptation and Vulnerability*. Contribution of Working Group II. Eds.: *McCarthy, J.J., Canziani, O.F., Leary, N.A., Dokken D.J., White K.S.*. Cambridge University Press, London.

Johns, T.C., Carnell, R.E., Crossley, J.F., Gregory, J.M., Mitchell, J.F.B., Senior, C.A., Tett, S.F.B., and *Wood, R.A.*, 1997: The second Hadley Centre coupled ocean-atmosphere GCM: model description, spinup and validation. *Climate Dynamics 13*, 103-134.

Jonsson, T., Johannesson, T., and *Källen, E.*, 1994: *Climate Changes Scenario for the Nordic Countries. A Preliminary Report.* Vedurstofa Islands, Orkustofnun, Icelandic Meteorological Office, National Energy Authority, OS-94030/VOD-04B.

Kadioglu, M., Sen, Z., and *Gultekin, L.*, 1999: Spatial heating monthly degree-day features and climatologic patterns in Turkey. *Theoretical and Applied Climatology 64(3-4)*, 263-269.

Kellomäki, S., 1993: Computations on the influence of changing climate on the soil moisture and productivity in Scotsh pine stands in southern and northern Finland. *Climatic Change 29*, 35-51.

Kharin, V.V. and *Zwiers, F.W.*, 2000: Changes in the extremes in an ensemble of transient climate simulations with a coupled atmosphere-ocean GCM. *J. Climate 13*, 3760-3788.

Kuivalainen, P., Forsius, J., and *Mäkinen, P.*, 1996: *Effects of Climate Change on the Production and Consumption of Electricity in Finland.* Imatra Voima OY, Environmental Protection Division, Vantaa, Finland.

Pope, V.D., Gallani, M.L., Rowntree, P.R., and *Stratton, R.A.*, 2000: The impact of new physical parameterisations in the Hadley Centre Climate model-HadCM3. *Climate Dynamics 16*, 123-146.

Quayle, R.G. and *Diaz, H.F.*, 1980: Heating degree-day data applied to residential heating energy consumption. *J. Applied Meteorology 19(3)* 241-246.

Roeckner, E., Bengtsson, L., Feichter, J., Lelieveld, J., and *Rodhe, H.*, 1999: Transient climate change simulations with a coupled atmosphere-ocean GCM including the tropospheric sulfur cycle. *J. Climate 12*, 3004-3032.

Sælthun, N.R., Aittoniemi, P., Bergström, S., Einarsson, K., Johannesson, T., Lindström, G., Ohsson, P.E., Thomsen, T., Vehviläinen, B., and *Aamodt, K.O.*, 1998: *Climate Change Impacts on Runoff and Hydropower in the Nordic Countries. Final report from the project "Climate Change and Energy Production"*, Copenhagen.

Soule, P.F. and *Suckling, P.W.*, 1995: Variations in heating and cooling degree-days in the South-eastern USA, 1960-1989. *Int. J. Climatology 15*, 355-367.

Starostova, M., 1999: Air temperature and heating period characteristics in south Bohemia (in Czech). *Hydrometeorologicky Ustav*, Prague, Czech Republic, 57-66.

Taylor, B.L., 1981: Population-weighted heating degree-days for Canada. *Atmosphere-Ocean 19*, 261-268.

Tistea, D., 1974: Computation and zoning of annual heating period duration and heating degree-days sum corresponding to inside and outside temperatures (in Romanian). *Studii de Climatologie 2*, 131-155.

Washington, W.M., Weatherly, J.W., Meehl, G.A., Semtner, A.J. Jr, Bettge, T.W., Craig, A.P., Strand, W.G. Jr, Arblaster, J., Wayland, V.B., James, R., and *Zhang, Y.*, 2000: Parallel climate model (PCM) control and transient simulations. *Climate Dynamics 16*, 755-774.

IDŐJÁRÁS

Quarterly Journal of the Hungarian Meteorological Service
Vol. 108, No. 2, April–June 2004, pp. 141–153

Tendencies in variability of gridded temperature and precipitation in Hungary (during the period of instrumental record)

Louise Bodri

Research Group on Geophysics and Environmental Physics, Hungarian Academy of Sciences, c/o Geophysics Department of Eötvös Loránd University, Pázmány P. sétány 1/C, H-1117-Budapest, Hungary; E-mail: bodri@pangea.elte.hu

(Manuscript received August 15, 2002; in final form March 7, 2003)

Abstract—Analysis of monthly variability was performed on two 100–150 years long grid-point series of temperature anomalies and precipitation from Central Europe, near Hungary. Increasing temperature during the 19th and 20th centuries has been accompanied by a decrease in monthly variability. Thus, at present the temperature evolves towards to more stable climate, especially in spring and summer. Lower variability is linked to more rapid winter warming. Slow decrease of precipitation together with the noticeable increase in precipitation variability is characteristic for the 20th century. The increase in precipitation variability is more rapid in summer. Observed climatic variability near Hungary is generally consistent with the patterns found for other European mid-latitude locations as well as with those predicted by Global Circulation Models (GCMs).

Key-words: temperature, precipitation, variability trends.

1. Introduction

Climate is variable on all time scales. For better understanding of the nature of the climate changes, attention is to be focused not only to the evolution of mean climate characteristics, but also to the changes in the climate variability, and to climate extremes. The necessity of including of the variability characteristics in the climate change studies has been demonstrated in several works (*Katz* and *Brown*, 1992; *Rebetez*, 1996; *Wilks* and *Riha*, 1996; and the references therein). A detailed understanding of climate variability is important to the prediction of extreme climatic events. It can be demonstrated that the frequency of climatic

extremes is more sensitive to the changes in variability rather than to the mean climate state (*Katz* and *Brown*, 1992). *Rebetez* (1996) has shown that climate variability is one of the most important characteristics in the human perception of climate. The potential response of the socio-economic fabrics of the global community to the changes in climate variability may be stronger than to the changes in climatic averages (*Rebetez*, 1996; *Wilks* and *Riha*, 1996), while these changes are completely obscured when examining only the evolution of mean characteristics.

One of the important fields of application of the variability investigations is the detection of possible forced (e.g., anthropogenic) climate trends. For example, in the face of the climatic change from the increased greenhouse gas concentrations in the Earth atmosphere, there is strong evidence that changes will occur not only in climatic mean state but also in their higher order moments. General Circulation Models (GCMs) associated with the build-up of greenhouse gases predict not only increase in temperatures but also a possible decrease in temperature variability (*McGuffie et al.*, 1999; *Karl et al.*, 1999). While a global trend of 0.3–0.6°C during the last century has been widely recognized (*Nicholls et al.*, 1996; *Hansen et al.*, 2001), changes in the climate variability have been less well studied or understood. Recent investigations of the surface air temperature (SAT) variability in fact revealed definite decreasing variability trends in SAT records (*Karl et al.*, 1995; *Moberg et al.*, 2000; *Rebetez*, 2001; *Yan et al.*, 2001, *Bodri* and *Cermak*, 2003). These studies admitted also, that the climate changes differently from one region to another; thus, changes in the SAT variability can be confidently diagnosed only on the base of wide regional studies. Such investigations can be used for the validation of the simulated models for various scenarios of greenhouse-gas emission and land use.

The situation is more complex with other associated climatic variables, such as precipitation, that also can be affected by the global warming phenomenon. Most of the existing models, like, e.g., recent investigations by *Hulme et al.* (1998), are oriented towards the influence of the global warming on the precipitation means. Precipitation sensitivity to the global warming for the land areas simulated in the above work by a set of eight HadCM2 models with different forcings achieved 1.5 to 2.5%/K over the period 1900–1996. These values imply 3–15 mm precipitation growth for the last century, and coincide well with the global land precipitation growth of 9 mm/100 years, calculated by *New et al.* (2001), from precipitation gauge data. This growth is relatively small in comparison with considerable precipitation variability. According to *New et al.* (2001) on the decadal time scale range of the global land precipitation oscillations achieves ± 40 mm from the century mean of 950 mm.

The pioneering investigations concerning precipitation variability were performed by *Houghton et al.* (1992), who summarized model results for

conditions under doubled carbon dioxide concentration, and conclude that there is some indication of increase of the precipitation rate in selected regions, which could be accompanied by the simultaneous increase in the variability of the precipitation. The simulations of 21st century climate by *Kattenberg et al.* (1996) using GCMs forced with increasing atmospheric concentrations of greenhouse gases also indicated an increase in the intensity of the hydrological cycle as global temperature increases, implying increase in total precipitation, in the number of wet days and days with extreme precipitation, as well as revealed an area dependence of the changes. These conclusions were further specified in the study by *Mearns et al.* (1995). Investigations of $2 \times CO_2$ influence conducted with a regional climate model (RegCM) nested in a GCM indicated the possibility of significant regional increase in precipitation variability (with or without changes in median intensity). In vast regions there may be larger and more significant changes in variability rather than in medians. The possibility of detectable alterations in precipitation variability with no and/or imperceptible changes in its mean characteristics hints the necessity to include the higher order moments in precipitation change assessments.

In present work we analyze 100–150 years long surface air temperature (SAT) and precipitation time series from the territory of Hungary in order to better understand the pattern of their variability variations. This work can contribute to a few previous investigations of climatic variability and somewhat complete still insufficient information on the regional variability changes.

2. Data

To investigate the patterns of variability, we used the gridded time series of SAT anomalies and precipitation for the territory of Hungary. Gridded data accumulate the effects of individual stations. These time series appear more smoothed, thus, the range of variability variations may be more narrow, than in the measured data, and the "explosions" of variability resulting from the local extreme events may be missed. On the other hand, general trends revealed by these data are of the area importance, and can serve for verification of variability trends obtained from original station data. Traditionally, long-term climatic data in Europe have consisted of monthly mean values. Such scale of aggregation is more suitable for the regional investigation. As it was mentioned by *Yan et al.* (2001), at the shorter time scale, e.g., daily, variability is quite local in character. This makes it relatively sensitive to any changes in local conditions, thus, it may serve as a good indicator of inhomogeneity in climatic series, rather than the real variability changes.

Data sets of SAT anomalies and precipitation were provided by the Climate Research Unit, University of East Anglia, Norwich UK (www.cru.uea.ac.uk).

The SAT data is a combination of land air temperature anomalies (*Jones*, 1994) and sea surface temperature anomalies (*Parker et al.*, 1995) on a 5° × 5° grid-box basis. This size is as best as possible merging the effect of the temperature gradients and data availability. The merging of the two datasets is discussed in *Parker et al.* (1994). Both components of the dataset are expressed as anomalies from 1961–90. The monthly data from the grid-box 45–50°N, 15–20°E embracing the period of 1856–1998 were used for the calculations. All stations were actively assessed for the homogeneity. Some of these corrections are site specific relating to moves of the instruments and exposure changes (one of the important errors is connected to urbanization effect around the sites), and some are nationally specific arising from observation time and methods used to calculate monthly means. The elaboration of the homogenized long-term climate data for Hungary was performed by *Szentimrey* (1997, 1999; see also http://omsz.met.hu/ismeretterjesztes/rendezvenyek/rendezveny_hu.html).

The most informative homogenized precipitation series for the 20th century are presented by *Hulme et al.* (1998) (see also updated version on www.cru.uea.ac.uk) as land precipitation amounts from 1900 to 1998, gridded at 2.5° latitude by 3.75° longitude resolution. Because of stronger spatial variability of the precipitation, a smaller box size would be preferable. The present size is stipulated by the data availability. The grid box with the center at 47.5°N, 18.75°E was used for calculations. The station data were corrected to exclude gauge biases due to changing place and gauge design. Data have been also subjected to additional homogeneity procedure reported by *Hulme* (1992). For example, they were screened for gross outliers and typographical errors. Both time series are presented in *Figs. 1* and *2* (top), respectively.

Temperature anomalies record contains definite linear warming trend of 0.65 ± 0.11 K/100 yr (*Fig. 1*). The amount of the 20th century warming is comparable with the values of 0.3–0.6 K/100 yr obtained for the global warming trend (*Nicholls et al.*, 1996; *Hansen et al.*, 2001). In order to perform seasonal analyses, original monthly temperature anomalies were stratified into four commonly defined seasons. Linear trends for the seasonalized data are shown in *Table 1*. Obtained slopes indicate far the largest warming in the winter season. Warming trends in spring and autumn are approx. two times lower than in winter, while the summer warming is very light. Such distribution indicates that the warming process happens through the loss of the coldest part of the year. The monthly precipitation contains a general decreasing linear trend of -5.9 ± 2.7 mm/100 yr (possibility of slightly drier conditions in future) existing at least from the beginning of the 20th century (*Fig. 2*). Decreasing trend is observable for all seasons, though, very slightly in summer. However, neither of these trends is statistically significant (*Table 1*).

3. Temperature and precipitation variability

The measure of variability used in the present study is based on the work by *Karl et al.* (1995) and is defined by the absolute value of the difference in precipitation between two adjacent periods of time. For the time series of T_1, T_2, T_3, ..., T_i, ... the measure of variability ΔT_N (N-point change) is defined as the absolute difference between the average of a sequence of measured values for N points that begins at point i and the average for the N-point long sequence beginning at point $(i+N-k)$

$$\Delta T_N = abs\left(\overline{T_i} - \overline{T_{i-k}}\right), \tag{1}$$

where

$$\overline{T_i} = \frac{1}{N}\sum_{m=i}^{i+N-1} T_m\,; \quad \overline{T_{i-k}} = \frac{1}{N}\sum_{m=i+N-k}^{i+2N-k-1} T_m\,. \tag{2}$$

For the time lag $k > 0$ there are partly overlapping running differences. The method above is free of some disadvantages of more conventional methods, such as the standard deviation, thus, e.g., prevents a confounding of high- and low-frequency variability (*Karl et al.,* 1995). Similarly to other measures of variability, N-point change characterizes the range of climatic variations. Low variability value means approx. the same conditions in the next time interval as in the previous one, while high variability corresponds to significant differences between the neighboring intervals. For example, high value of monthly precipitation variability means that, e.g., a dry month was immediately followed by an extremely wet month.

The measure of variability was calculated successively for the whole time series to obtain variability measure. The value of N was chosen as one, corresponding to the monthly averaging intervals. *Figs. 1* and *2* (bottom) show the monthly variability curves for the SAT anomalies and precipitation, respectively. As it can be seen, climate warming during the 20th century has been accompanied by the reduction in monthly variability, predicted by the most of GCMs. Time series of SAT variability exhibits general decreasing trend of -0.20 ± 0.06 K/100 yr that implies approx. 15% present decrease in SAT variability in comparison with the beginning of the 20th century. Observed decrease in temperature variability can be explained by the more rapid winter warming in comparison with the summer period. While the summer period shows practically no long-term warming trend, the winter warming is approx. two times higher than the estimated global value. A larger increase in the winter temperatures than in the summer temperatures results in a substantial decline in

the annual temperature range (difference between summer and winter temperatures), thus, in the corresponding decrease in variability. An analysis of variability trends for different seasons shows, that the SAT variability decreases during the warmest part of the year from spring to autumn and is insignificant in the winter season (*Table 1*).

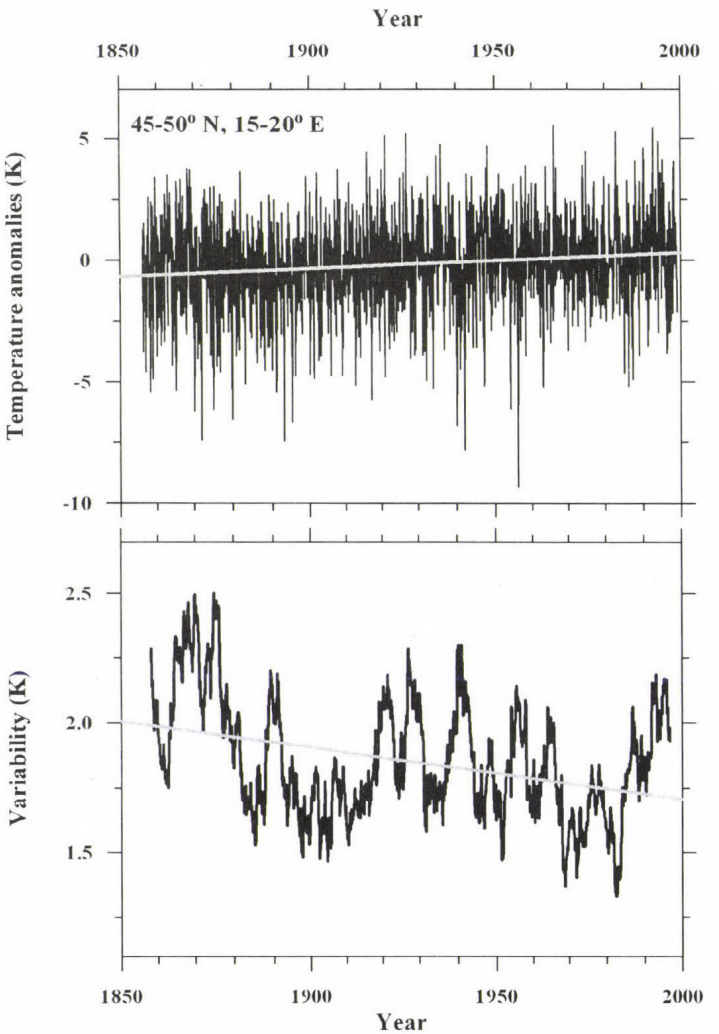

Fig. 1. Top: Time series of monthly SAT anomalies for the historical data set grid box centered at 47.5°N, 17.5°E (*Jones*, 1994). *Bottom:* Variability pattern for monthly SAT series. Low frequency changes are highlighted by a Gaussian filter corresponding roughly to 4-year moving averages. Thick lines represent the linear trends.

Time series of precipitation variability (*Fig. 2*, bottom) exhibits general increasing trend of 5.1 ± 0.9 mm/100 yr. The variability of precipitation increases for all seasons, but most rapidly in the summer period (*Table 1*). This hints at more variable summer precipitation in the future, and because of existing strong coupling of extreme and monthly precipitation, when the wettest day of the month

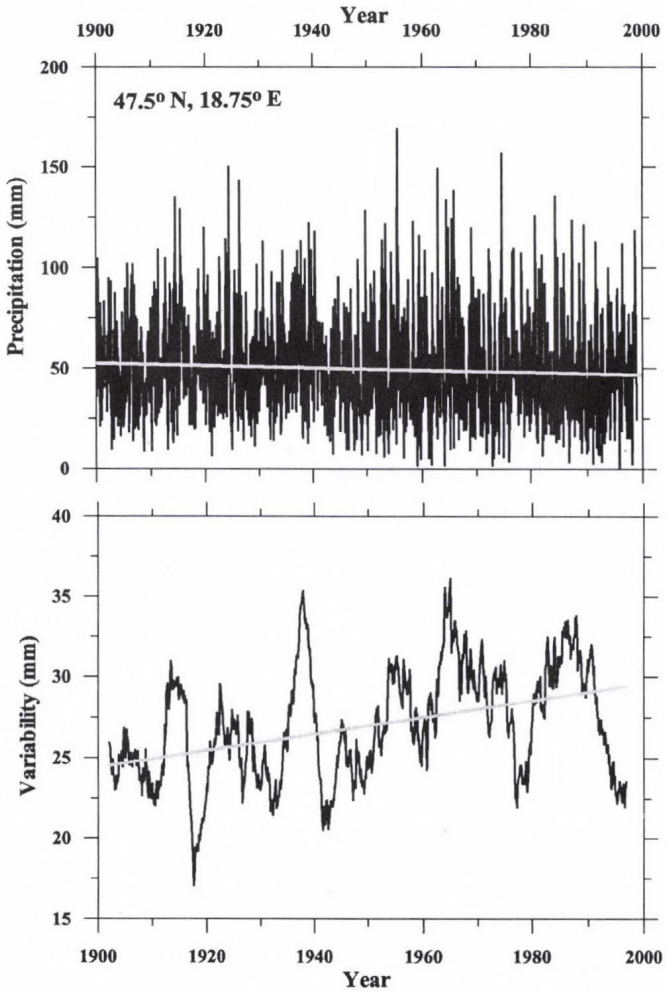

Fig. 2. Top: Time series of monthly precipitation for the historical monthly precipitation data set grid box centered at 47.5°N, 18.75°E (*Hulme et al.*, 1998). *Bottom:* Variability pattern for monthly precipitation. A Gaussian filter corresponding roughly to 4-year moving averages highlights low frequency changes.

contributes considerably to the total sum (see e.g., *Heino et al.*, 1999), at increasing probability of precipitation extremes in the summer period. Similar intensification of the hydrological cycle was obtained in several early works. *Karl et al.* (1995) analyzed daily precipitation data from the U.S. for the period 1910–1996, and found approx. 10% increase in annual precipitation, that occurred in most cases, because of a greater number of rainy days, with the greatest contribution arising from an increase in the number of extreme precipitation events, indicating an increased precipitation variability. The most recent investigations of precipitation trends in the 20th century by *New et al.* (2001) based on the gridded data sets revealed secular increasing trends in different domains, e.g., 8.9 and 41.6 mm/100 yr for global data set and in the mid-latitudes (40–60°N) of the Northern Hemisphere, respectively, in many regions accompanied by the increase of the wet spells frequency. They concluded that over much of the global land area (including also Europe) there was an increase in the intensity of precipitation events on the scales from 1 day to 3 months.

Table 1. Linear trends in monthly SAT anomalies (1856–1998) and precipitation (1900–1998) and their variability. (Trends are given in K/yr for SAT anomalies and/or for their variability and in mm/yr for precipitation and its variability, respectively.)

Period	Winter	Spring	Summer	Autumn	Year
SAT	0.013±0.003	0.006±0.002	0.002±0.002	0.005±0.002	0.006±0.001
SAT variability	0.0001± 0.0012	-0.0034± 0.0015	-0.0030± 0.0012	-0.0020± 0.0017	-0.0020± 0.0006
Precipitation	-0.038±0.041	-0.098±0.049	-0.018±0.054	-0.083±0.061	-0.059±0.027
Precipitation variability	0.020±0.012	0.028±0.013	0.107±0.022	0.019±0.019	0.051±0.009

Variability calculations above were completed by spectral analysis. Traditional Fourier analysis picks up signals changing in both frequency and time, features that are more closely related to real patterns of climate change. While the monthly precipitation itself does not possess any significant periodicity except for the ordinary 1 and 1/2 year waves (see results of the spectral analysis of precipitation time series; *Fig. 3*, top), the variability pattern exhibits definite quasi-cyclicity. Part of these oscillations can be attributed to the large scale forcing mechanisms, such as the NAO and AO (*Bodri et al.*, 2004). "Explosions" of variability generally coincide with the enhanced monthly precipitation; thus, imply an increased risk of extreme precipitation. However, in the present case an observed quasi-cyclicity does not contain any predictive possibility. As it can be seen in *Fig. 3* (bottom), the power spectrum of precipitation variability obeys a

power law form over a given frequency range of $E(f) \sim f^{-b}$, where f is the frequency, characteristic for the scale invariant (fractal) behavior. Spectral exponent b equals to -1.97 ± 0.08, thus, practically coincides with 2. Series with $b = 2$ represent ordinary Brownian noise, which is known as a purely random process. Thus, the observed cycles are quite far from periodic; for example, they cannot be extrapolated as the sample lengthens, cannot be related to the temporal periodicity of the precipitation forming process, etc.

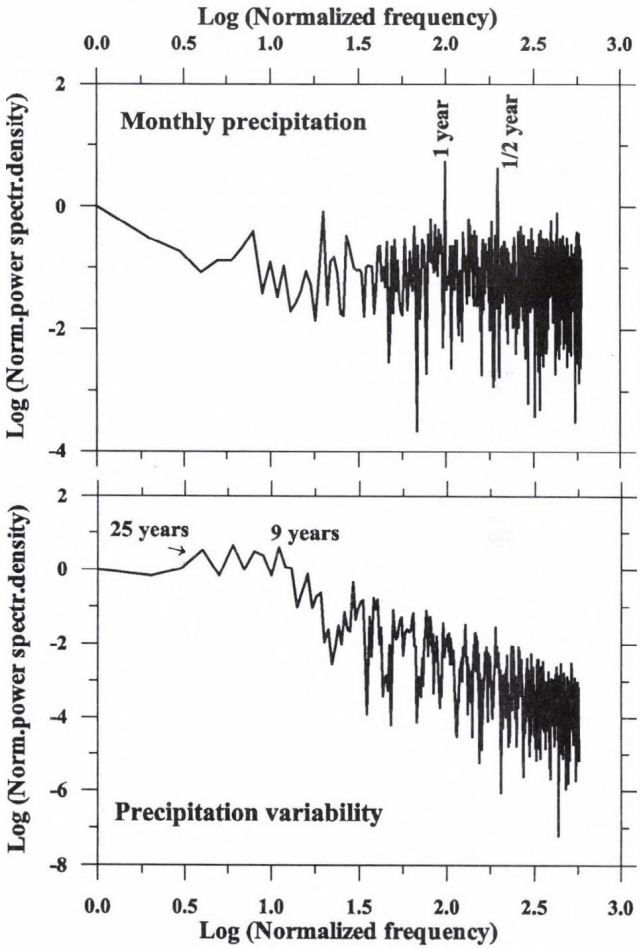

Fig. 3. Top: Power spectrum of the precipitation time series. The values are relative: the frequencies are normalized to the lowest frequency in the spectrum, the power spectral density to that at the lowest frequency. *Bottom:* Power spectrum of the precipitation variability time series.

4. Conclusions

As it was shown in several works, the quantities that are to be used to describe climate change scenarios are not only the mean characteristics of the climate but also higher order statistical moments, such as variability. The study of climate variability gives a more comprehensive summary of climate than conventional climate averages. Results of variability-related studies have many practical applications, since the impact of the variability changes on the environmental and associated socio-economic systems may be more perceptible than the slow changes in the mean characteristics. The investigations of variability, likewise the investigation of general trends, can be further used for the validation of the simulated models for various scenarios of greenhouse-gas emission and land use. The GCMs, that have been applied to the problem of the effect of increasing CO_2 levels combined with aerosol increases, predict not only global increase of surface air temperature, but also changes in the precipitation rate, however, they do not give an unequivocal picture of how the higher moments might be expected to change. Variability changes, especially, the changes in the hydrological cycle, are likely depending on the investigated spatial domain. In present work, two climatic data sets were collected for Hungary in order to characterize the variability of temperature and precipitation over the period of historical records. Analyses presented in this work lead to the following conclusions.

- Since the middle of the 19th century, monthly SAT temperatures in Hungary have warmed by 0.9°C (in comparison with the 0.3–0.6°C global value; *Nicholls et al.*, 1996; *Hansen et al.*, 2001). Simultaneously, the temperature variability decreased by approx. 15%. The decrease in temperature variability occurred due to the fact, that on a seasonal basis, the bulk of the warming in Hungary has taken place in the colder periods of the year (fall-spring); only very light warming was observed in summer.

- On monthly scale, precipitation slightly decreased over the 20th century. For the same period there was approx. 20% increase in precipitation variability, which occurred because of the less rapid decrease in the summer precipitation amounts, than in the winter amounts. On seasonal scale, variability increase is far more pronounced in summer. If this tendency will further continue, the summer may become far more variable season than the rest of the year, including the possibility of heavy precipitation extremes and increased risk of summer floods. It should be mentioned, however, that the situation in Hungary is far less marginal, than in some other regions of Europe. *Fig. 4* shows time series of monthly precipitation together with the calculated variability pattern for the grid box with the center at 50°N and 15°E, which coincides approximately with the position of Prague (the Czech

Republic). Variability shows general increasing trend of 6.0±0.3 mm/100 yr since at least the beginning of the 20th century. Except for this general increasing trend, the range of variability variations also increased significantly, that can be attributed to the more rapid growth of the variability maxima than the minimum values (14.8 and 4.2 mm/100 yr, respectively). Rapid growth of variability maxima implies the corresponding

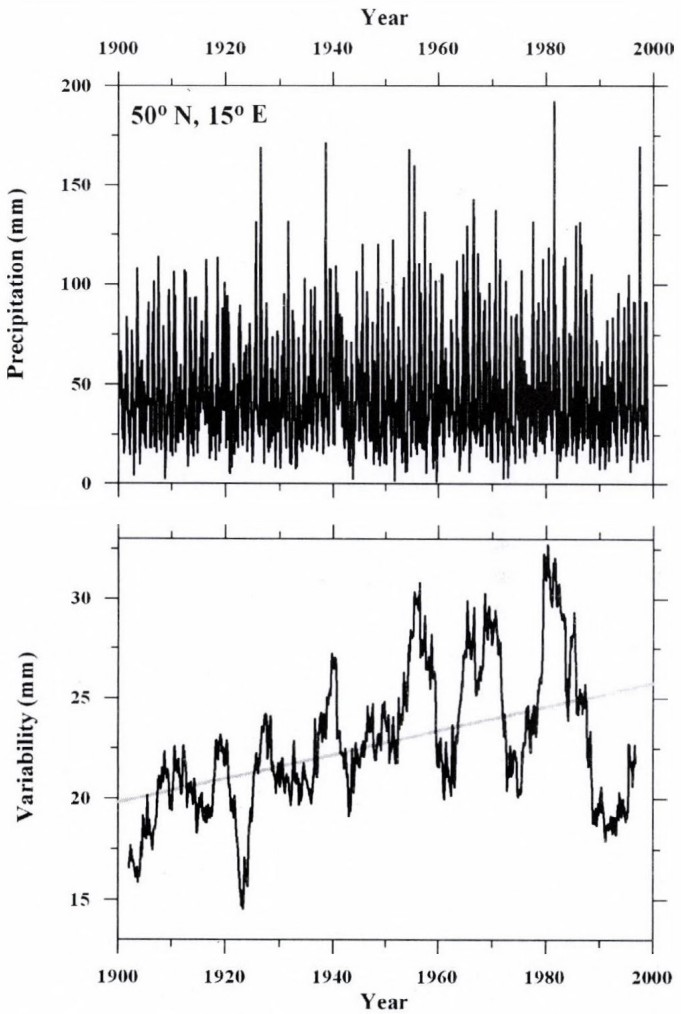

Fig. 4. Top: Time series of monthly precipitation for the historical monthly precipitation data set grid box centered at 50°N, 15°E (*Hulme et al.*, 1998). *Bottom:* Variability pattern for monthly precipitation.

increase of occurrence and intensity of extreme precipitation events. The oscillations of variability have become more pronounced after the year 1950. At least for the last 50 years, interdependence between extreme precipitations, increased range of precipitation variability, and the summer floods at the river Vltava can be traced (e.g., events of Julies 1954, 1981 and 1997; *Kakos*, 1997; as well as the recent floods of August 2002). On the contrary, with the precipitation record from the Czech Republic, the range of precipitation variability oscillations in Hungary even somewhat decreased for the last 50 years.

- As with many other areas of the world, the findings of the present study are broadly consistent with the projections made by $2 \times CO_2$ models of global warming.

Acknowledgements—Author thanks the Climatic Research Unit, University of East Anglia, Norwich, UK, for kindly providing the data used in this study.

References

Bodri, L. and *Cermak, V.*, 2003: High frequency variability in recent climate and the North Atlantic Oscillation. *Theor. Appl. Climatol. 74*, 33-40.

Bodri, L., Cermak, V., and *Kresl, M.*, 2004: Trends in precipitation variability: Prague (the Czech Republic). *Climate Change* (in press).

Hansen J., Ruedy, R., Sato, M., Imhoff, M., Lawrence, W., Easterling, D., Peterson, T., and *Karl, T.*, 2001: A closer look at United States and global surface temperature change. *J. Geophys. Res. 106*, 23947-23963.

Heino, R., Brazdil, R., Forland, E., Tuomenvirta, H., Alexandersson, H., Beniston, M., Pfister, C., Rebetez, M., Rosenhagen, G., Rösner, S., and *Wibig, J.*, 1999: Progress in the study of climatic extremes in Northern and Central Europe. *Climatic Change 42*, 151-181.

Houghton, J.T., Callander, B.A., and *Varney, S.K.* (eds.), 1992: *Climate Change 1992.* The Supplementary Report to Climate Change: The IPCC Scientific Assessment. Report prepared for the IPCC Working Group I. Cambridge Univ. Press, Cambridge.

Hulme, M., 1992: A 1951-80 global land precipitation climatology for the evaluation of GCMs. *Climate Dynamics 7*, 57-72.

Hulme, M., Osborn, T.J., and *Johns, T.C.*, 1998: Precipitation sensitivity to global warming. Comparison to observations with HadCM2 simulations. *Geophys. Res. Lett. 25*, 3379-3382.

Jones, P.D., 1994: Hemispheric surface air temperature variations: a reanalysis and an update to 1993. *J. Climate 7*, 1794-1802.

Kakos, V., 1997: Hydrometeorological analysis of historical flood in the year 1897 in connection with the catastrophic floods in the Czech Lands in the beginning of September 1890 and in Morava River in July 1997 (in Czech). *Meteorologicke zpravy 50*, 191-196.

*Karl, T.R., Knight, R.*W., and *Plummer, N.*, 1995: Trends in high frequency climate variability in the twentieth century. *Nature 377*, 217-220.

Karl, T.R., Nicholls, N., and *Ghazi, A.*, 1999: CLIVAR/GCOS/WMO workshop on indices and indicators for climate extremes. Workshop summary. *Climatic Change 42*, 3-7.

Kattenberg, A., Giorgi, F., Grassl, H., Meehl, G.A., Mitchell, J.F.B., Stouffer, R.J., Tokioka, T., Weaver, A.J., and *Wigley, T.M.L.*, 1996: Climate models: projections of future climate. In *Climate Change 1995: The Science of Climate Change* (eds.: *J.T. Houghton, L.G. MeiroFilho, B.A. Callendar, A. Kattenberg*, and *K. Maskell*). Cambridge Univ. Press, Cambridge, UK, 285-357.

Katz, R.W. and *Brown, B.G.*, 1992: Extreme events in a changing climate: variability is more important than averages. *Climatic Change 21*, 289-302.

McGuffie, K., Henderson-Sellers, A., Holbrook, N., Kothavala, Z., Balachova, O., and *Hoekstra, J.*, 1999: Assessing simulations of daily temperatures and precipitation variability with global climate models for present and enhanced greenhouse climates. *Int. J. Climatol. 19*, 1-26.

Mearns, L.O., Giorgi, F., McDaniel, L., and *Shields, C.*, 1995: Analysis of daily variability of precipitation in a nested regional climate model: comparison with observations and doubled CO_2 results. *Global Planet. Change 10*, 55-78.

Moberg, A., Jones, P.D., Barriendos, M., Bergström, H., Camuffo, D., Cocheo, C., Davies, T.D., Demareé, C., Martin-Vide, J., Mangeri, M., Rodriguez, R., and *Verhoeve, T.*, 2000: Day-to-day temperature variability trends in 160- to 275-year-long European instrumental records. *J. Geophys. Res. 105*, 22849-22868.

New, M., Todd, M., Hulme, M., and *Jones, P.*, 2001: Precipitation measurements and trends in the twentieth century. *Int. J. Clim. 21*, 1899-1922.

Nicholls, N., Gruza, G.V., Jousel, J., Karl, T.R., Ogallo, L.A., and *Parker, D.E.*, 1996: Observed climate variability and change. In *Climate Change 1995: The Science of Climate Change* (eds.: *J.T. Houghton, L.G. MeiroFilho, B.A. Callendar, A. Kattenberg*, and *K. Maskell*). Cambridge Univ. Press, Cambridge, UK, 133-192.

Parker, D.E., Jones, P.D., Bevan, A., and *Folland, C.K.*, 1994: Interdecadal changes of surface temperature since the late 19th century. *J. Geophys. Res. 99*, 14373-14399.

Parker, D.E., Folland, C.K., and *Jackson, M.*, 1995: Marine surface temperature: observed variations and data requirements. *Climatic Change 31*, 559-600.

Rebetez, M., 1996: Public expectation as an element of human perception of climate change. *Climatic Change 32*, 495-509.

Rebetez, M., 2001: Changes in daily and nightly day-to-day temperature variability during the twentieth century for two stations in Switzerland. *Theor. Appl. Climatol. 69*, 13-21.

Szentimrey, T., 1997: Statistical procedure for joint homogenization of climatic time series. *Proc. Seminar for Homogenization of Surface Climatological Data,* Budapest, Hungary, 47-62.

Szentimrey, T., 1999: Multiple analysis of series for homogenizaton (MASH). *Proc. Second Seminar for Homogenization of Surface Climatological Data,* Budapest, Hungary; WMO, WCDMP-No.41, 27-46.

Wilks, D.S. and *Riha, S.J.*, 1996: High-frequency climatic variability and crop yields. *Climatic Change 32*, 231-235.

Yan, Z., Jones, P.D., Moberg, A., Bergström, H., Davies, T.D., and *Yang, C.*, 2001: Recent trends in weather and seasonal cycles: An analysis of daily data from Europe and China. *J. Geophys. Res. 106*, 5123-5138.

GUIDE FOR AUTHORS OF *IDŐJÁRÁS*

The purpose of the journal is to publish papers in any field of meteorology and atmosphere related scientific areas. These may be

- research papers on new results of scientific investigations,
- critical review articles summarizing the current state of art of a certain topic,
- short contributions dealing with a particular question.

Some issues contain "News" and "Book review", therefore, such contributions are also welcome. The papers must be in American English and should be checked by a native speaker if necessary.

Authors are requested to send their manuscripts to

Editor-in Chief of IDŐJÁRÁS
P.O. Box 39, H-1675 Budapest, Hungary

in three identical printed copies including all illustrations. Papers will then be reviewed normally by two independent referees, who remain unidentified for the author(s). The Editor-in-Chief will inform the author(s) whether or not the paper is acceptable for publication, and what modifications, if any, are necessary.

Please, follow the order given below when typing manuscripts.

Title part: should consist of the title, the name(s) of the author(s), their affiliation(s) including full postal and E-mail address(es). In case of more than one author, the corresponding author must be identified.

Abstract: should contain the purpose, the applied data and methods as well as the basic conclusion(s) of the paper.

Key-words: must be included (from 5 to 10) to help to classify the topic.

Text: has to be typed in double spacing with wide margins on one side of an A4 size white paper. Use of S.I. units are expected, and the use of negative exponent is preferred to fractional sign. Mathematical formulae are expected to be as simple as possible and numbered in parentheses at the right margin.

All publications cited in the text should be presented in a *list of references*, arranged in alphabetical order. For an article: name(s) of author(s) in Italics, year, title of article, name of journal, volume, number (the latter two in Italics) and pages. E.g., *Nathan, K.K.,* 1986: A note on the relationship between photo-synthetically active radiation and cloud amount. *Időjárás 90,* 10-13. For a book: name(s) of author(s), year, title of the book (all in Italics except the year), publisher and place of publication. E.g., *Junge, C. E.,* 1963: *Air Chemistry and Radioactivity.* Academic Press, New York and London. Reference in the text should contain the name(s) of the author(s) in Italics and year of publication. E.g., in the case of one author: *Miller* (1989); in the case of two authors: *Gamov* and *Cleveland* (1973); and if there are more than two authors: *Smith et al.* (1990). If the name of the author cannot be fitted into the text: *(Miller,* 1989); etc. When referring papers published in the same year by the same author, letters a, b, c, etc. should follow the year of publication.

Tables should be marked by Arabic numbers and printed in separate sheets with their numbers and legends given below them. Avoid too lengthy or complicated tables, or tables duplicating results given in other form in the manuscript (e.g., graphs)

Figures should also be marked with Arabic numbers and printed in black and white in camera-ready form in separate sheets with their numbers and captions given below them. Good quality laser printings are preferred.

The text should be submitted both in manuscript and in electronic form, the latter on diskette or in E-mail. Use standard 3.5" MS-DOS formatted diskette or CD for this purpose. MS Word format is preferred.

Reprints: authors receive 30 reprints free of charge. Additional reprints may be ordered at the authors' expense when sending back the proofs to the Editorial Office.

More information for authors is available: antal.e@met.hu

Information on the last issues: http://omsz.met.hu/irodalom/firat_ido/ido_hu.html

Published by the Hungarian Meteorological Service

Budapest, Hungary

INDEX: 26 361

HU ISSN 0324-6329